

This is an Open Access document downloaded from ORCA, Cardiff University's institutional repository:<https://orca.cardiff.ac.uk/id/eprint/171384/>

This is the author's version of a work that was submitted to / accepted for publication.

Citation for final published version:

Gullapalli, Anirudh, Aburakhis, Taha, Featherston, Carol , Pullin, Rhys , Morini, Lorenzo and Kundu, Abhishek 2025. A cyberphysical structural health monitoring framework for threshold-free active signal detection and classification on the edge. *Journal of Nondestructive Evaluation, Diagnostics and Prognostics of Engineering Systems* 8 (2) , 021003. 10.1115/1.4066196

Publishers page: <http://dx.doi.org/10.1115/1.4066196>

Please note:

Changes made as a result of publishing processes such as copy-editing, formatting and page numbers may not be reflected in this version. For the definitive version of this publication, please refer to the published source. You are advised to consult the publisher's version if you wish to cite this paper.

This version is being made available in accordance with publisher policies. See <http://orca.cf.ac.uk/policies.html> for usage policies. Copyright and moral rights for publications made available in ORCA are retained by the copyright holders.



# A cyberphysical structural health monitoring framework for threshold-free active signal detection and classification on the edge

Anirudh Gullapalli<sup>1</sup>, Taha Aburakhis<sup>1</sup>, Carol Featherston<sup>1</sup>, Rhys Pullin<sup>1</sup>,  
Lorenzo Morini<sup>2</sup>, and Abhishek Kundu\*<sup>1</sup>

<sup>1</sup>*School of Engineering, Cardiff University,, The Parade, Queen's Buildings, Cardiff, CF24 3AA, United Kingdom ,*

<sup>2</sup>*Department of Mechanical, Chemical and Materials Engineering, University of Cagliari, Cagliari, 09123, Italy ,*

## Contents

<b>1</b>	<b>Introduction</b>	<b>2</b>
<b>2</b>	<b>Cyberphysical systems</b>	<b>4</b>
2.1	Physical layer . . . . .	4
2.2	Digital Layer . . . . .	5
<b>3</b>	<b>Materials and methods</b>	<b>6</b>
<b>4</b>	<b>Results and Discussions</b>	<b>11</b>
4.1	Time-History Waveform Study . . . . .	12
4.2	Amplitude Response Analysis . . . . .	13
4.3	Signal conditioning and time-frequency transformations . . . . .	15
4.4	In-line signal classification on-the-edge . . . . .	18
4.5	Wave velocity calculation and uncertainty quantification . . . . .	21
4.6	Slowness curves and wave mode identification . . . . .	26
<b>5</b>	<b>Conclusions</b>	<b>27</b>

## Abstract

The increased focus on predictive maintenance of safety-critical engineering structures requires an onboard structural health monitoring system which is reliable and robust to provide accurate predictions of health metrics of structures while also being efficient and streamlined to facilitate autonomous data processing and real-time decision-making capabilities. An onboard structural health monitoring system with the capability to continuously monitor and interrogate a structure, describe its current state, and assess the operational risks of the degraded structure needs to be developed and matured so that it can

---

\*Email: [kundua2@cardiff.ac.uk](mailto:kundua2@cardiff.ac.uk)

be deployed in practical, real-time monitoring scenarios. This would constitute a cyberphysical system in structural health monitoring. A cyberphysical system is a mechanism that is controlled by computer-based algorithms integrated with the internet and working with users. There exists a physical domain that is under examination and its digital counterpart which is informed by data from the physical as well as simulation models. While there exist multiple surveys on the overarching advantages, limitations, and potential of realizing a cyberphysical system, innovation on structural systems, in-line signal processing and damage event detection in the context of a cyberphysical system, especially from an experimental point of view is still in its infancy. In this work, we implement a versatile cyberphysical framework - CyberSHM using a sparse network of transducers and an edge computing device. Hosted on the structure of interest, the transducers possess the capability to interrogate the structure continuously, periodically, on-demand or autonomously when triggered by damage or an unplanned acoustic event. In addition, the device also possesses efficient on-edge feature extraction and signal classification capabilities which serve as crucial starting points for further damage analysis and characterization on the digital layer.

**Keywords.** cyberphysical system, structural health monitoring, guided wave, smart sensing, signal processing, composite structure, machine learning

## 1 Introduction

Structural health monitoring (SHM) technologies need to keep pace with the rapid structural and functional design innovations in materials, design, and topology. Innovative structural design leads to new challenges in SHM, especially when monitoring in-service structures with the aim of minimizing industrial downtime. Also, with the advent of several technology enablers like edge computing devices, advanced machine learning techniques and the industrial internet of things, amongst others, the industry is getting closer to the vision of continuous monitoring systems within a data-rich environment to realize the goal of predictive maintenance of their critical assets [1]. State-of-the-art engineering designs usually focus on complex high-performance lightweight structures which exhibit complex failure modes. This makes detecting and predicting damage initiation, growth and maintenance intervention planning challenging. SHM techniques such as acoustic emission (AE) [2], [3] and ultrasonic guided wave (UGW) [4], [5] have been employed to assess the health of a structure in conjunction with advanced signal post-processing techniques to handle large volumes of continuous monitoring data. Limited computing ability and sensor memory space can be an issue while handling such large volumes of data collected in real-time in-service SHM. The most essential task required by an SHM system is monitoring and deciding on the structural condition using the essential features extracted from data available for post-processing and decision-making. Therefore, this data should be reliable enough. If the essential features embedded in the original signal are not lost in the process of compression and reconstruction, compressive sensing (CS) can be considered to be employed in an SHM system for real-time monitoring and decision making [6]–[8]. The essential signal features help to map out the existence, location, and severity of damage and are crucial to identify and choose the most optimum features to describe the current health state of a structure [9], [10]. Sensitivity of signal features to damage characteristics, size and severity, sensor location optimisation, multiple damage type identification, uncertainty quantification and machine learning have been highlighted as crucial areas of research to achieve an industry grade SHM system [11]–[13]. With an increase in the complexity of engineering structures, volume of data being collected and the requirement of real-time decision making,

automation of SHM systems is crucial. Machine learning (ML) algorithms can serve to recognize and classify data based on a training dataset using advanced algorithms. Over the past years, many researchers have shed light on the influence of ML algorithms on SHM. Multiple versatile ML frameworks including neural networks [14], Gaussian processes [15] and regression models [16] amongst others have been established and used to map different AE signal features [17]–[20] and ultrasonic guided wave signal features [21]–[23] to damage properties and been found to have the potential to accurately identify different damage types in engineering structures. While these studies highlight the innovation in developing ML-frameworks with functionalities including damage localisation, multi-class damage classification and adaptability to variable operating conditions, it is important to note that these models rely heavily on prior knowledge of damage location and a dense training data set.

A data-driven approach can be a robust alternative to compensate for such externalities in the absence of prior knowledge about changes in signal characteristics with external conditions. Implementing data-based techniques and concepts of information entropy are also useful in sensor positioning optimisation to achieve the best performance with a sparse sensor array [24]–[26]. Moreover, incorporating physics knowledge to ML algorithms rather than relying solely on data-driven approaches, has shown enhanced performance in damage detection and characterisation [27], [28]. However, extensive sensor data required for training an ML algorithm poses a challenge in real-time feature extraction, entailing high computational complexity and cumbersome equipment. Bayesian inference has been employed in numerous studies to detect multiple damage cases in structures without prior knowledge, although it is computationally expensive [29]–[31]. Incorporating surrogate models into this framework has proven essential for enhancing computational efficiency by establishing a statistical relationship between input and output parameters, thus reducing the number of numerical simulation iterations [32], [33]. While most research has primarily focused on the computational domain, there has been little innovation towards developing a framework that utilizes state-of-the-art edge computing technologies to design a reliable in-service UGW data acquisition and management system [34]. The quality of acquired data is essential for the optimal performance of machine learning algorithms. For safety-critical engineering applications, continuous autonomous monitoring presents a significant challenge, as it involves processing large volumes of data and making autonomous decisions in real-time. This paper addresses these challenges by establishing a cyber-physical system (CPS)-based structural health monitoring (SHM) framework that leverages cost-effective edge devices with on-the-edge data processing and decision-making capabilities, focusing on essential acoustic event representative data acquisition and processing. The study emphasizes the CyberSHM physical layer’s signal acquisition, classification, and processing capabilities to identify the earliest arriving ultrasonic guided wave mode. This represents a foundational step towards developing a non-intrusive autonomous SHM system. Subsequent research will build on this framework by isolating the fundamental ultrasonic guided wave modes through a model-informed and experimental data-driven approach. Analyzing the changes in their modal properties due to structural damage and mapping these changes to parameterized damage metrics will establish reliable damage signatures. These signatures will provide engineers with detailed insights into the current health state of the structure, enabling the identification of optimal maintenance intervention points. This groundwork is essential for advancing towards a physics-informed, robust, and non-intrusive SHM system capable of real-time decision-making. The approach of integrating both physical and digital layers can be a promising solution for SHM systems in the field of prognostics and health monitoring. Over the past few years, CPS has drawn the attention of industry and academia alike with the promise to improve quality of life and facilitate technological advances in critical areas such as emergency



response [35], [36], healthcare [37], [38], energy [34], [39] and financial services [40], [41] in addition to engineering and science. Researchers from various disciplines have explored the concept of CPS with emphasis on the challenges, advantages and disadvantages associated with employing a CPS in various applications. It is well-established from these literatures that CPS holds great potential as a means of connecting individual systems and entities into a cohesive unit, offering advanced capabilities, and addressing important requirements such as reliability, versatility, robustness, and flexibility [42]–[46]. In the context of damage detection and health monitoring of aircraft fuselage [47], [48], bridges [49], pipelines [50] and wind turbine blades [51], coverage area, sensor location optimisation, energy efficiency and harvesting were identified as challenges and key research areas. More work on using CPS to investigate different damage types can be found in [52], [53].

The remainder of the paper is structured as follows. [section 2](#) presents the conceptual background of the envisioned cyberphysical framework – CyberSHM, the major research challenges and their applications with regards to SHM. [section 3](#) outlines the experimental setup, methodology and data post-processing techniques employed in this study. Results and discussions are provided in [section 4](#), followed by conclusions in [section 5](#).

## 2 Cyberphysical systems

CPS refers to the integration of physical devices, systems and the digital world through computer algorithms, networks, and software. This integration allows for the seamless exchange of information between the physical and digital layers, allowing physical devices to sense, control and respond to the real world whilst being informed by various numerical and ML algorithms. The integration of engineering principles and practices from various fields including mechanical, environmental, civil, electrical biomedical, chemical, and aeronautical engineering with computer science principles and practices, presents a significant challenge in the field of CPS. The interplay between the physical and cyber layers is at the core of this challenge, rather than the mere unification of the two. A CPS is the realisation of the intersection of the physical and cyber layers and not the union as shown in [figure 1](#). There are two main layers of a CPS: the physical layer and the digital layer. The physical layer consists of the physical devices and systems that interact with the real world, while the digital layer is a representation of the physical layer that allows for simulations and predictions. In the following section, we elucidate the functions and interactions of each layer of the envisioned CPS – CyberSHM.

### 2.1 Physical layer

Consider the physical layer in CyberSHM, which comprises of a structural system which is subjected to external loads, and variable operating conditions which influence its behaviour. The factors related to variations in loads, environmental conditions, and structural properties are parameterized and can be incorporated into the structural model. Under the action of loads and excitations, the structural system generates a response, which can include displacements, strains, stresses, and dynamic responses amongst others.

The digital signal processing (DSP) hardware, which is part of the physical layer, acquires signals from the structural system, sends interrogation or control signals, and monitors the structural response. The DSP hardware communicates with the sensors used in the structural system and is used for deducing information on all relevant structural or control parameters. The main operations performed on the DSP platform include data acquisition, digital signal

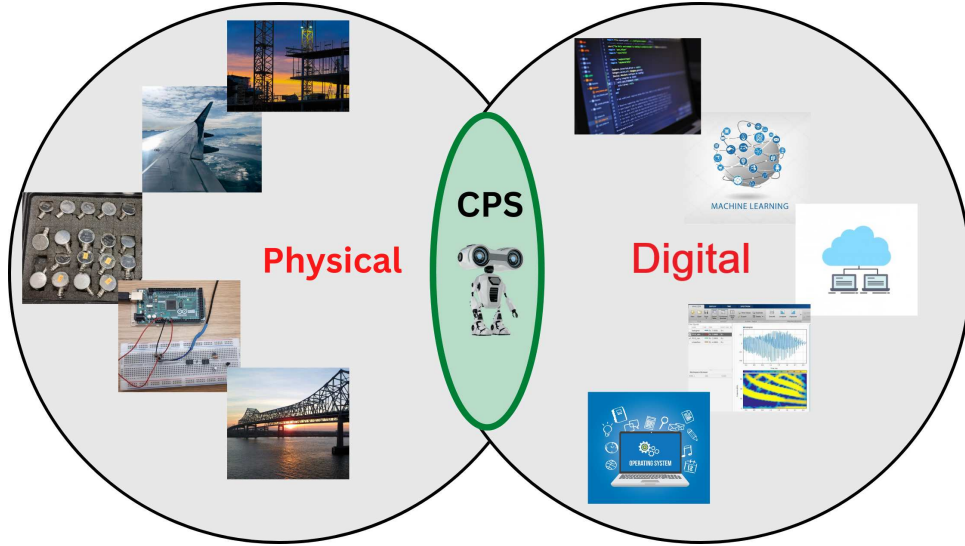


**Figure 1:** A set-theoretic representation of the *physical* and *digital* components of a cyberphysical system (CPS) which can be deployed for active monitoring and prognostics of safety-critical engineering systems.

processing, and interrogation of the structure. With the collected raw signals, the structural and operational parameters can be inferred based on the study of essential signal features like frequency response, power spectral density, time of flight for ultrasonic applications and wave dispersion/scattering study, amongst others.

## 2.2 Digital Layer

In addition to the physical layer, a digital equivalent layer exists in CyberSHM. A digital equivalent of the structure being monitored under the action of operational loads with varying operational conditions can be simulated with a number of latent parameters. The latent parameters provide useful information of the structural properties which are not directly measurable. Realising the digital equivalent is computationally expensive and based on an idealised, simplified set of assumptions with regards to the physical behaviour of the system, although it is not necessarily the real behaviour. To make the digital models respond in real-time and evolve with the measured states of the structure, a computationally feasible approach is to train a surrogate model offline to map the measured signal parameters to the parameterised structural properties and deployed in-situ to work with real-time data for active monitoring. An additional surrogate model can be generated based on mapping experimentally measured input-output data so that the model can adapt to dynamic changes in the environment and the load conditions.

To bring the experimentally measured data and digital layers together and incorporate the complementary information and uncertainties in each, we create a model informed digital twin. The model informed digital twin provides the unique advantage of quantifying uncertainties of complementary nature such as the aleatoric uncertainties associated with measurement noise and the epistemic uncertainties associated with modelling assumptions [54]. When human factors are also incorporated into this framework, a human-centred model-informed digital twin is obtained which can incorporate expert knowledge and subjective opinion.

### 3 Materials and methods

In this paper, a detailed analysis of the physical layer of CyberSHM is presented. The research is centred around the development and implementation of a versatile framework for an edge device which will enable the device to 1) actuate any thin-walled plate-like structure with a user-defined actuation signal, 2) record signals generated by the structural system and 3) perform signal conditioning and post-processing operations locally on-edge and relay the extracted essential features to the digital layer for further classification and characterisation. The CyberSHM physical layer is controlled by two algorithms running in parallel as illustrated in [figure 2](#) – the interrogation algorithm and the file-check algorithm. The interrogation algorithm excites the structure of interest with a user-defined signal via a sparse array of transducers and saves the data on the edge computing device. Triggered by the onset of a new batch of data, the file-check algorithm classifies the acquired data into one of the two classes- the acoustic event representative (AER) signal or non-AER signal. In this context, an acoustic event refers to any event that may jeopardize the safety of the structure of interest, such as cracks, delaminations, or tool drops. The non-AER signal is eliminated from the edge computing device while the AER signal is subjected to feature extraction algorithm(s) following which the essential features are relayed to the digital layer for subsequent condition monitoring tasks. This tackles one of the main challenges faced by continuous and autonomous monitoring systems, which is extracting valuable information from high bit-rate data streams.

This workflow will represent a significant step towards the realisation of a fully integrated CPS. To achieve this, there is a need for command line tools that demonstrate computational efficiency and compatibility with a diverse range of tightly-knit rigorous ML algorithms. In the sections that follow, a clear demonstration of this physical layer is provided, highlighting typical inferences and observations obtained from signal processing operations. Conclusive remarks are drawn based on the findings, elucidating how this work can contribute to the realisation of an integrated CPS tailored for SHM.

The experimental setup involved the use of two 12-layered carbon fiber reinforced epoxy composite (CFRC) panels, each measuring  $(500 \times 500 \times 3)$  mm. These panels featured the layup of  $[+45_3 / -45_3]_S$  and were manufactured using USN 150 B pre-preg plies through vacuum bagging process. The plies were cut at  $+45^\circ$  and  $-45^\circ$  to produce 6 laminae of each orientation. The plies were then stacked and debulked after every five layers to ensure proper consolidation and to prevent void formation. Once stacking and debulking processes were completed, the panel was cured in the autoclave, *Aeroform ltd.* composite curing system in accordance with the curing cycle shown in [figure 3](#).

CFRCs find utility in aircraft design, contributing to strong yet lightweight structural components such as wings and fuselages, as well as in the automotive industry for crafting lightweight body panels and bumpers. Moreover, their versatility extends to civil engineering applications such as bridge decks and structural support columns in buildings, where the demand for a combination of strength, stiffness and impact resistance is prominent [\[55\]](#). Additionally, they are instrumental in the production of high-performance sporting equipment including golf clubs, tennis rackets and surfboards [\[56\]](#), [\[57\]](#). In this study, one CFRC panel was utilized as a control sample, and the other was modified to simulate delaminations. Specifically, two Teflon inserts, each measuring  $(30 \times 30 \times 0.02)$  mm, were introduced to replicate delaminations, designated as D1 and D2. D1 represents a symmetric delamination located between the 6th and 7th plies, whereas D2 represents an asymmetric delamination situated between the 2nd and 3rd plies. The experimental setup and delamination locations are illustrated in [figure 4](#) and [figure 5](#), respectively. Note that  $t_c$  is the variable used to denote the thickness of the sample.

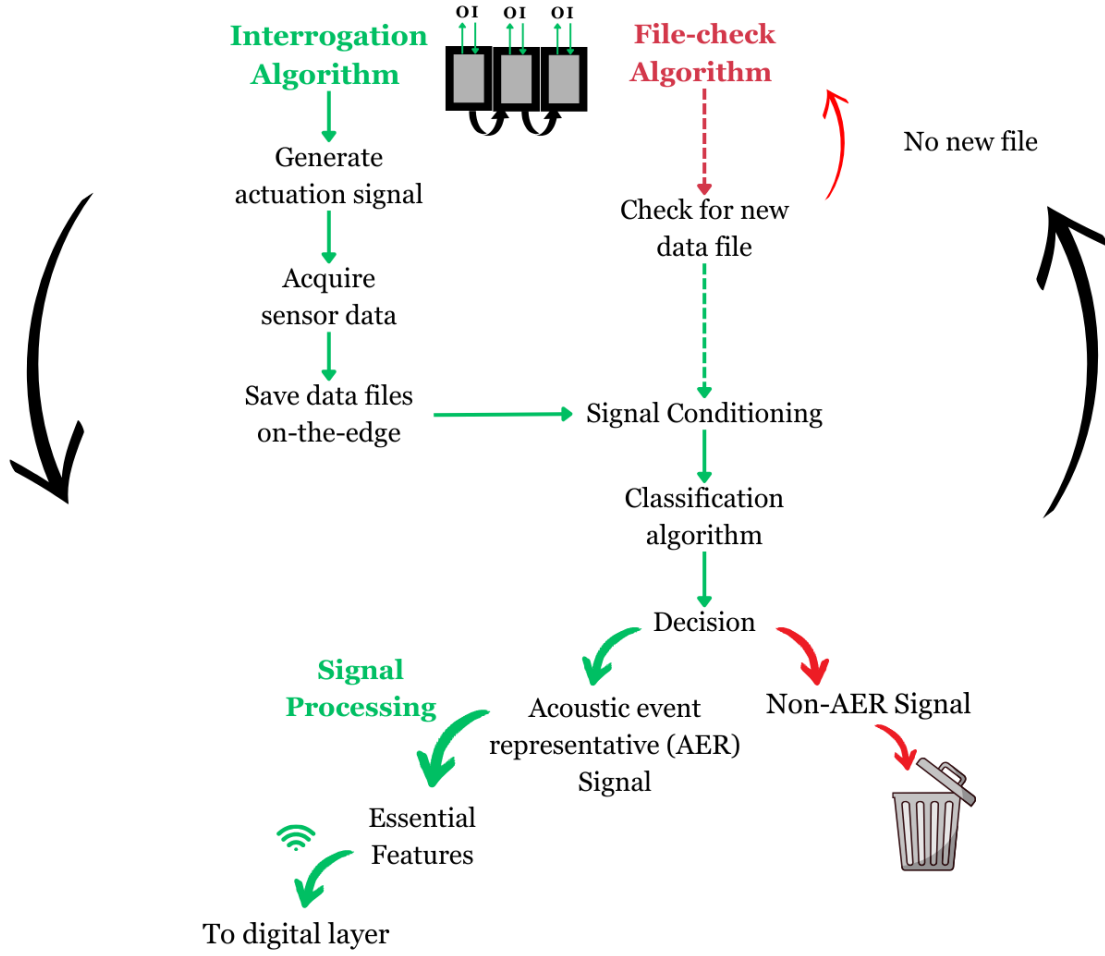


**Figure 2:** Process flow of signal acquisition and processing algorithms operating on the edge device constituting the CyberSHM physical layer.

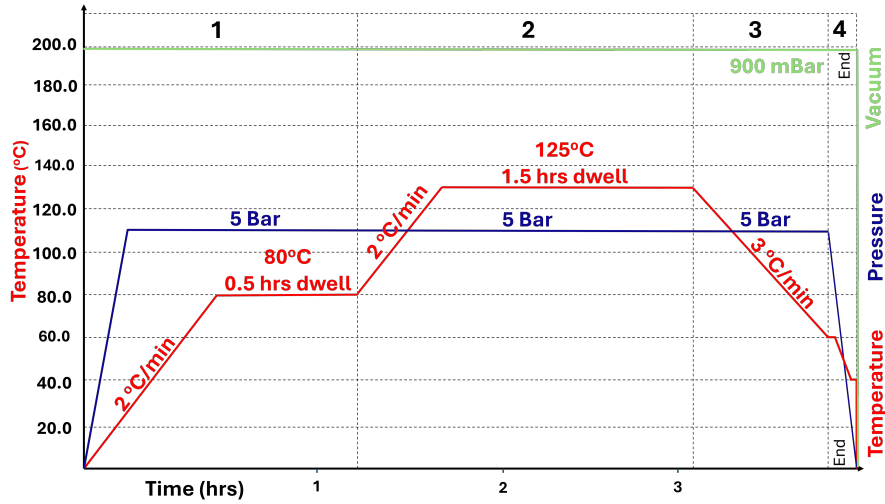


**Figure 3:** Curing cycle employed to the debulked 12-layered USN 150 B [ $+45_3 / -45_3$ ]<sub>S</sub> layup to fabricate the test samples.

To interrogate the samples, a smart node was utilized, comprising of an edge computing



Interrogation algorithm	<ul style="list-style-type: none"> <li>• Establish a secure connection–1 to the edge device with its unique IP address via an SSH protocol.</li> <li>• Set trigger condition: threshold-based trigger, signal generator trigger or no trigger condition.</li> <li>• Set sampling rate for signal acquisition</li> <li>• Define actuation signal profile with mathematical function, number of cycles, window function, sweeping frequency range.</li> <li>• Set actuation amplitude level.</li> <li>• <b>WHILE</b> trigger condition is true <ul style="list-style-type: none"> <li>– Acquire data.</li> <li>– Save data (.csv,.mat) in a folder on the edge device.</li> </ul> </li> </ul>
File-check algorithm	<ul style="list-style-type: none"> <li>• Establish a secure connection–2 to trigger the file-check algorithm script remotely on the edge device.</li> <li>• Set the status variable flag = 1.</li> <li>• Scan the local folder for new files.</li> <li>• <b>while the status variable is 1</b> <ul style="list-style-type: none"> <li>– <b>IF</b> the local folder accumulates a fresh batch of data (.csv/.mat files). <ul style="list-style-type: none"> <li>– send to classification algorithm.</li> <li>– <b>IF</b> the recorded data is classified as an AER signal. <ul style="list-style-type: none"> <li>– perform signal processing operations (as outlined in <a href="#">figure 22</a>) to extract essential features and relay them to the cloud server.</li> </ul> </li> <li>– <b>ELSE</b> <ul style="list-style-type: none"> <li>– purge the file.</li> </ul> </li> <li>– <b>ELSE</b> <ul style="list-style-type: none"> <li>– scan folder for new data files.</li> </ul> </li> </ul> </li> </ul> </li> <li>• Once data acquisition is complete, set flag to 0.</li> </ul>

**Table 1:** Tabular representation of the simultaneous interrogation and file-check algorithms deployed on the edge device.

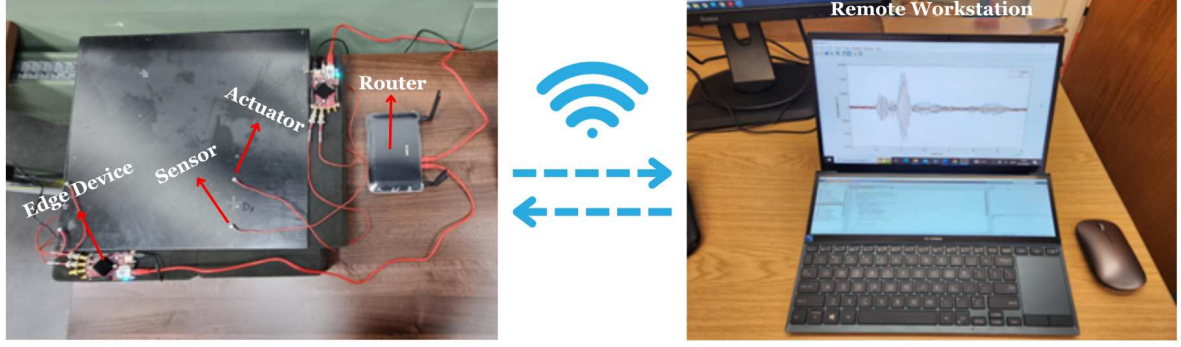


**Figure 4:** Experimental setup consisting of the CFRC sample interrogated by an edge device with two NANO30 transducers and a remote workstation.

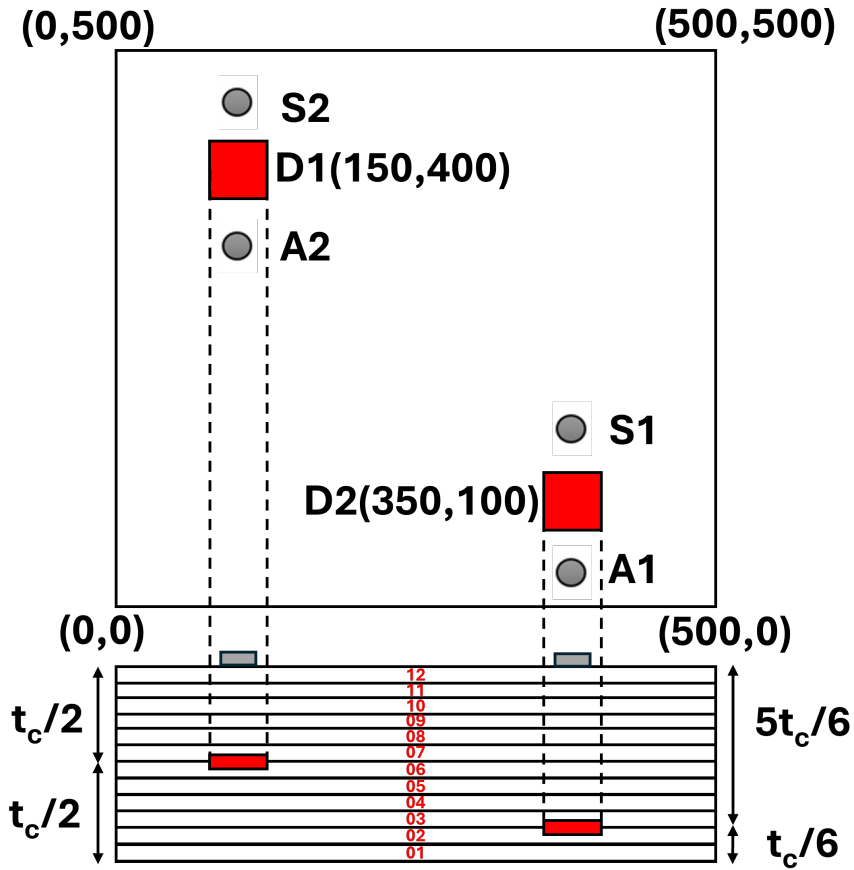


**Figure 5:** Diagram of  $(500 \times 500 \times 3)$  mm sample with symmetric D1 and asymmetric D2  $(30 \times 30 \times 0.02)$  mm delamination locations and transducer placement.

device (Red Pitaya STEMLab 125-14 referred to as edge device henceforth) and two NANO30 transducers serving as a sensor and an actuator. For actuation, the NANO30 transducers along with a wideband amplifier were used to inject a 2V peak-to-peak, Hanning windowed, five cycle sinusoidal wave with an amplification factor of ten. The transducers were attached to the panel using a drop of PC60 Cyanoacrylate adhesive and the data was collected at a sampling rate of 15.6MHz. A product datasheet provides valuable insights into a sensor's specifications and capabilities; however, it may not reflect its performance in a specific application. Identifying

an optimal frequency range for a sensor used to interrogate a particular sample is essential to ensure data accuracy, reliability, and overall quality. If the frequency range is unsuitable, the sensor may not perform as expected or provide the required level of detail, leading to suboptimal application performance. Therefore, a frequency response analysis was conducted, directly measuring the sensor's response to various frequencies. 150 – 300 kHz was determined to be the best suited frequency range for the current application as the sensor performance and the structure's sensitivity to the applied actuation signals were optimum in this range as evident in [figure 6](#).

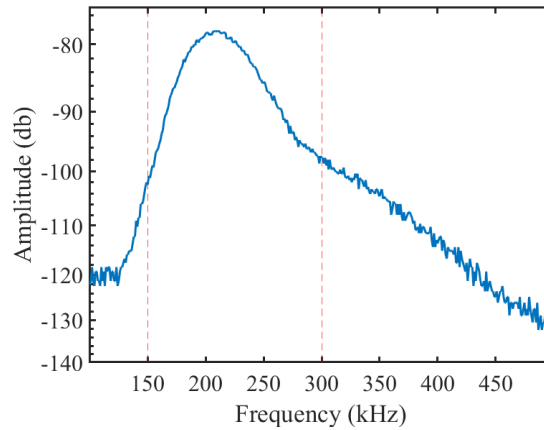


**Figure 6:** Frequency response of the sample to applied 2Vpp, Hanning windowed, 5-cycle sinusoidal signal excited at monotonic frequencies from 100kHz – 500kHz in steps of 1kHz.

The optimal frequency range is determined by a synergy of factors, including the structural sensitivity to specific actuation frequencies and the transducer's performance across the considered range of actuation frequencies. In the first set of experiments, both samples were subjected to an actuation frequency band of 150kHz to 300kHz with a step size of 1kHz. The objective was to detect and differentiate the pristine sample from the damaged sample. A streamlined workflow was established using a code developed with standard commands for programmable instruments (SCPI) [58], enabling seamless communication with the edge device through a Python interface. The developed code was designed to be ergonomic and efficient, allowing the experiment to be carried out by specifying the device IP-address, lower and upper limits, and the increment interval of actuation frequency. The versatile workflow facilitated continuous, periodic, or on-demand interrogation of the sample, with the ability to communicate with multiple edge devices if required. After the edge device collected the signals, post-processing algorithms were applied to the recorded data. These algorithms process the recorded signals to generate meaningful results using certain parameters that can be mapped to describe damage characteristics. The results obtained from this experiment are explained in [sections 4.1-4.2](#).

In the second set of experiments, the workflow was extended to incorporate three daisy-chained edge devices, with one device serving as the master and the others as slaves. All devices were connected to a router, allowing secure wireless access through SSH. To capture signals with varying signal-to-noise ratios (SNR), a linear array of transducers was deployed, each positioned at different distances from the actuator. The time-history waveforms from each transducer were converted into high-resolution time-frequency scalograms and classified into essential acoustic event representative signal and non-essential signal categories using an in-line classification algorithm. The outcomes of this experiment are discussed in detail in [section 4.4](#).

In the third set of experiments, transducers were strategically attached to the pristine panel in a semi-circular array. The primary objective was to analyze the wave velocity of the propagating waves along multiple directions and identify the earliest arriving guided wave mode. The actuating transducer was positioned at the center, while the sensing transducers were located at specific angles  $0, \frac{\pi}{4}, \frac{\pi}{2}, \frac{3\pi}{4}$  and  $\pi$  on the panel as illustrated in [figure 7](#). The experimentally generated slowness curves, which represented the inverse of wave velocity, were compared with those obtained from a semi analytical finite element (SAFE) model. This comparison helped identify and ascertain the earliest arriving elastic wave mode. The results obtained from this experiment are explained in [section 4.5](#) and [section 4.6](#).

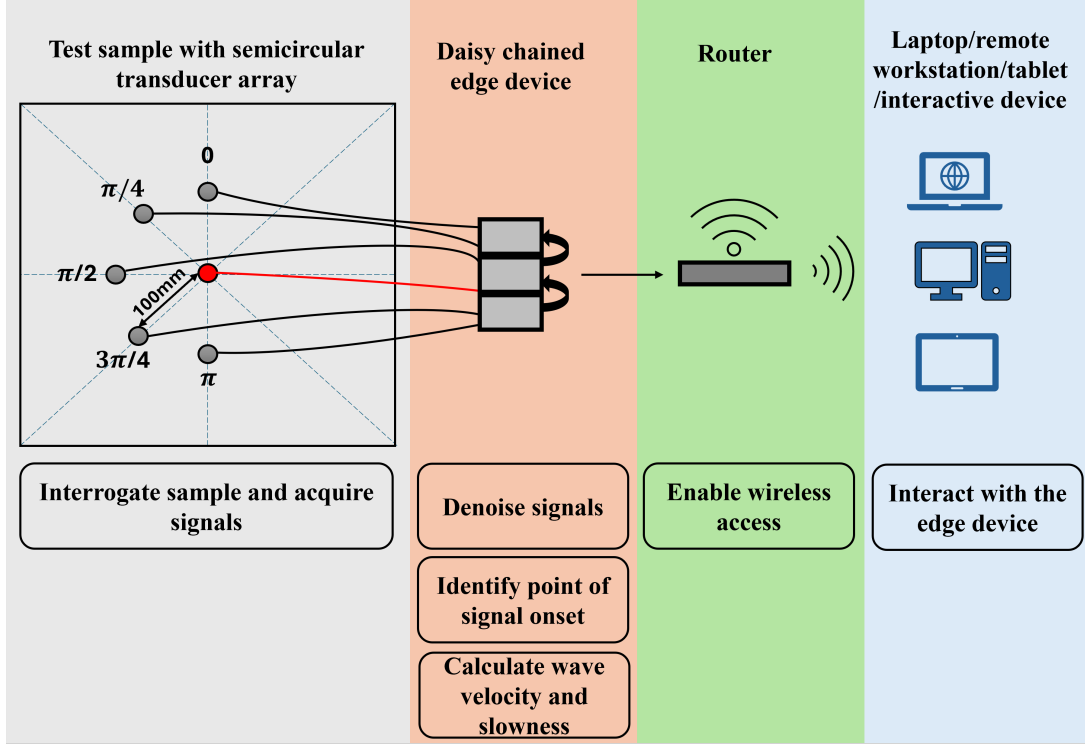


**Figure 7:** Transducer array and process flow of the daisy chained edge device used for slowness analysis and earliest arriving UGW mode identification in [section 4.6](#).

## 4 Results and Discussions

The acquired signals were subjected to a series of signal conditioning and processing operations. In the first stage, CNN was employed to categorize the acquired signals into either non-AER signals or AER signals on the edge. Non-AER signals were effectively eliminated. Subsequently, the AER signals were subjected to, time-history waveform inspection, amplitude comparison, frequency response analysis, Fast Fourier Transforms (FFT), Short Time Fourier Transforms (STFT), Daubechies 4 wavelet-based denoising, Akaike Information Criterion (AIC) based precise signal onset identification and slowness curve analysis aimed at distinguishing the pristine from the damaged panel and identifying distinct damage signatures for D1 and D2. This extensive signal acquisition and processing framework sheds light on both the structural system and the DSP platform, effectively constituting the physical layer of the CPS. Moreover, this framework offers the flexibility to accommodate more complex

signal processing algorithms, allowing it to adapt its functionality and meet specific requirements effectively. This flexibility enhances the system's versatility and broadens its potential applications. The following sections provide a comprehensive analysis of the acquired data, elucidating the observed trends and features in the processed signals.

## 4.1 Time-History Waveform Study

As a first level of damage detection, the time-history waveforms shown in [figure 8](#) were visualized to understand the influence of the two delamination types on the signal amplitudes and phases. Two significant observations emerged from this analysis: a substantial decrease in amplitude in the presence of damage and a noticeable delay in the arrival of the damaged signal compared to the healthy signal. To explain the reason behind these phenomena, it is crucial to understand how the damage influences the waveguide and the nature of interactions of the ultrasonic guided wave (UGW) modes with the waveguide. It is important to note that the structure under consideration is a thin-walled structure and the ultrasonic guided waves will propagate in the form of standing wave modes across the thickness  $t_c$  of the panel and propagating wave modes along its length. It can be considered that a delamination divides the composite panel into two sub-laminates between which the wave modes are split [\[59\]](#).

Delamination in a composite panel creates an impedance mismatch in the direction of propagation of the wave due to localized differences in the material properties and continuity of the waveguide. The structural acoustic impedance of the delaminated section differs from that of the pristine section on either sides of the delamination. Impedance mismatch at the interfaces of distinct sections of the waveguide has a significant effect on the acousto-ultrasonic wave due to partial reflection and scattering of the waves. This is manifested in the alteration of amplitudes and energy distributions of the various modes in the acoustic waveform.

It is evident that the signals originating from the symmetric delamination D1 exhibit a more pronounced loss of amplitude when compared to the signals from the asymmetric delamination D2. Delamination D1 is located at a depth of  $\frac{t_c}{2}$ , dividing the composite panel into two sub-laminates of equal thickness as shown in [figure 9](#). When the ultrasonic modes propagate through the D1 region, they encounter the delamination boundary which introduces an impedance mismatch in the direction of propagation. This impedance mismatch acts as a barrier to wave mode propagation reflecting and scattering away a major portion of the signal and transmitting only a fraction of it which is eventually picked up by the transducers. This leads to a significant loss of energy and consequently, the amplitude and the velocity of the UGW signal is considerably reduced in the presence of D1.

On the other hand, the asymmetric delamination D2 is situated at a depth of  $\frac{5t_c}{6}$ , dividing the panel into two sub-laminated of thicknesses  $\frac{5t_c}{6}$  and  $\frac{t_c}{6}$ . In this case, the transmission coefficient associated with D2 remains relatively high since the sublaminates affected by damage is largely pristine (83.33%) and hence the impedance mismatch between the pristine and damaged regions is relatively low. This implies that a significant portion of the signal can pass through the delamination without being heavily attenuated. As a result, the amplitude of the UGW signal from D2 experiences only a marginal decrease in comparison to the pristine signal. The difference in the extent of amplitude attenuation between D1 and D2 can be attributed to the depth and location of the delaminations with respect to the neutral axis. D1, being located closer to the central axis, causes a higher impedance mismatch and disrupting the wave propagation more significantly.

The visualisation of the time-history waveforms therefore provided valuable insights into the influence of delaminations on the amplitude and arrival time of the collected signals. The



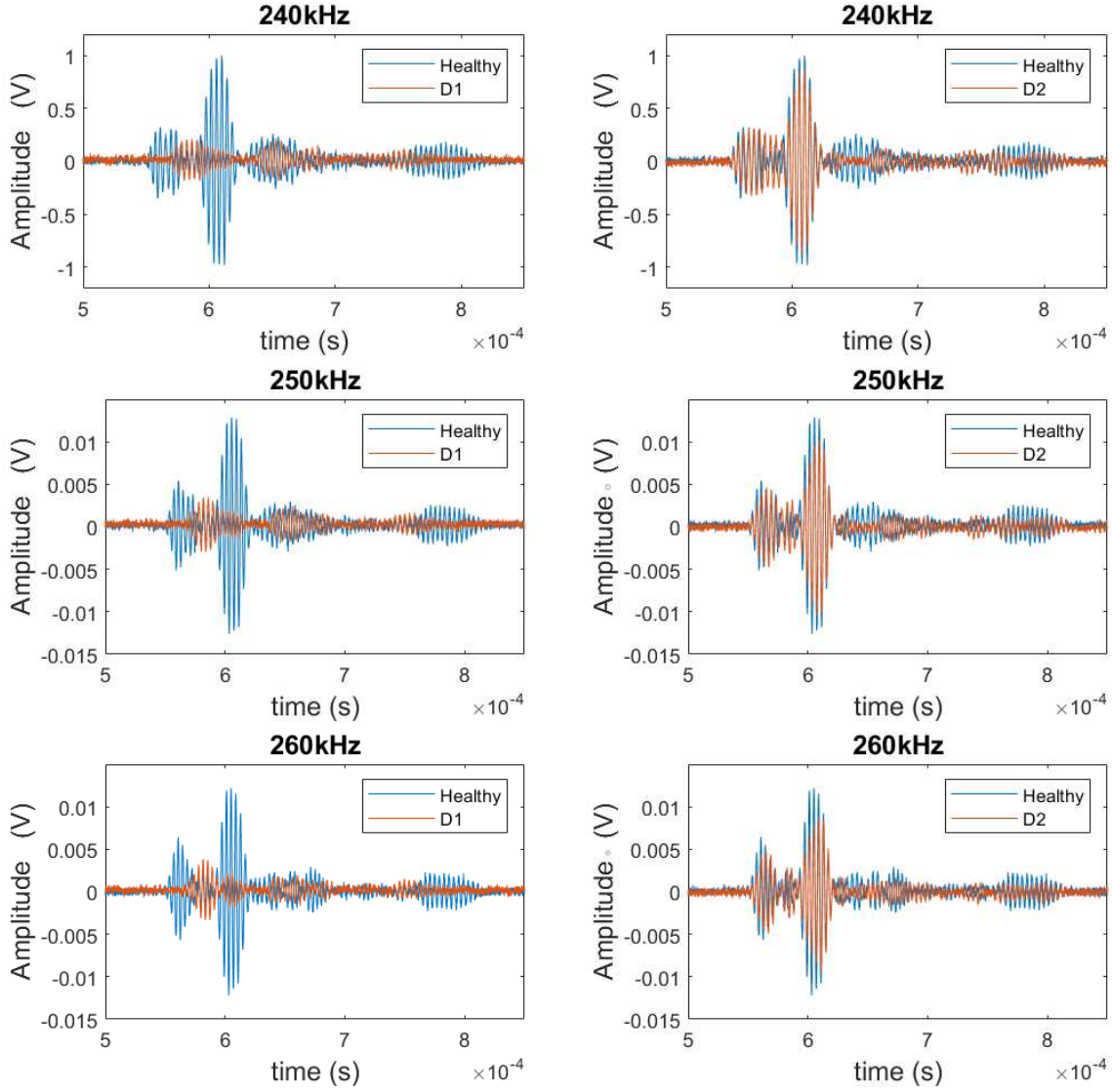


**Figure 8:** Pristine vs. symmetrically delaminated D1 and pristine vs. asymmetrically delaminated D2 time-series signal comparisons at 240kHz, 250kHz and 260kHz

observed loss of amplitude and delayed arrival time of the damaged signals compared to the healthy signals can be ascribed to the presence of delaminations, which introduce impedance mismatches between the pristine and the damaged regions of the panel in the direction of the propagation. The difference in the extent of the amplitude attenuation between D1 and D2 can be attributed to their respective depths and locations within the panel relative to the central axis. This understanding leads to the subsequent amplitude response analysis, where the distinct behavior of the delaminations in attenuating the UGW amplitude is analysed over a range of actuation frequencies.

## 4.2 Amplitude Response Analysis

The amplitude response analysis depicted in [figure 10](#) provides further insights into the behavior of the delaminations, specifically regarding their impact on the propagation of UGW modes. By comparing the amplitude responses of the delaminations D1 and D2 to the pristine sample's amplitude response, a clear distinction can be observed. Initially, the amplitude response of

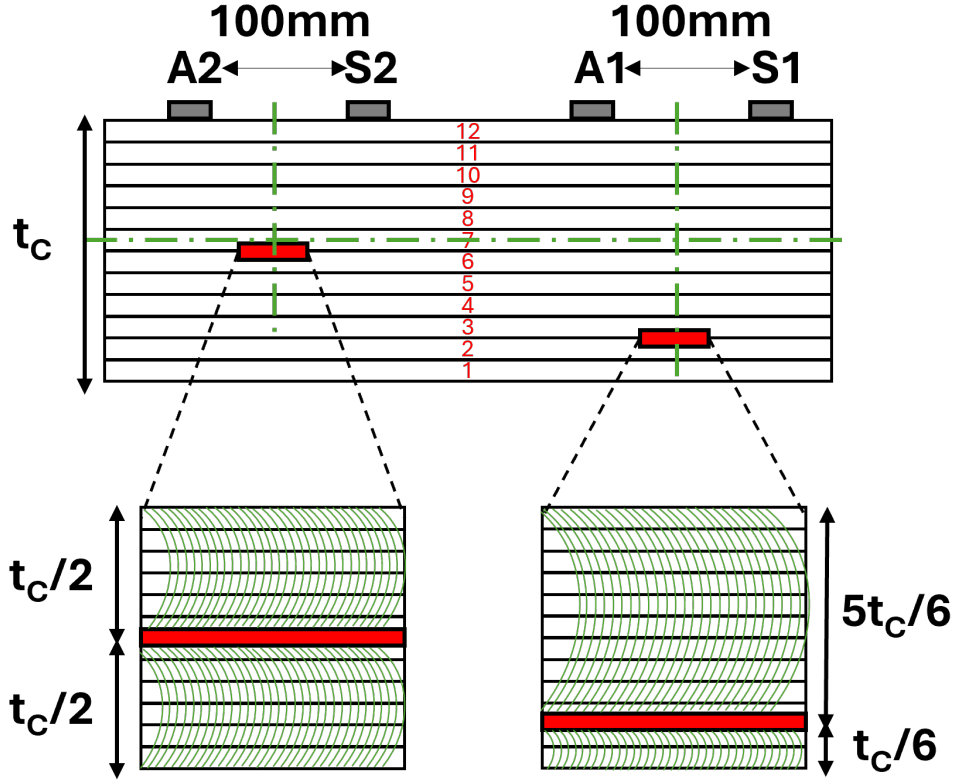


**Figure 9:** Pictorial representation of ultrasonic guided wave-mode splitting for the asymmetric delamination between layers 2 and 3 and the symmetric delamination between layers 6 and 7.

D2 closely mirrors that of the healthy case, suggesting that the presence of D2 does not introduce a substantial impedance mismatch, allowing the UGW modes to propagate with minimal attenuation. However, as the actuation frequency increases, a noticeable discrepancy emerges between the amplitude responses of D2 and the healthy case. At higher actuation frequencies, there is an increase in the number of oscillations occurring over a given distance resulting in energy loss due to UGW modes being susceptible to a higher degree of reflection and scattering. These dissipative mechanisms appear to dominate the effect of the minor impedance mismatch, explaining the observed discrepancy at higher actuation frequencies. In contrast, the amplitude response of D1 demonstrates a significant and consistent lower amplitude compared to both D2 and the pristine cases. The impedance mismatch induced by D1 has a dominant influence on the amplitude attenuation characteristics over the entire selected range of actuation frequencies, unlike D2. In summary, the amplitude response analysis highlights distinct effects of delaminations D1 and D2 on the amplitude of UGW signals. The presence of D1 induces a significant impedance mismatch, leading to a pronounced attenuation of the amplitude, while D2 exhibits a relatively minor amplitude drop due to a smaller impedance mismatch. These findings underscore the importance of considering the depth, location and resulting impedance mismatch when assessing the influence of the delaminations on the propagation characteristics of UGW.

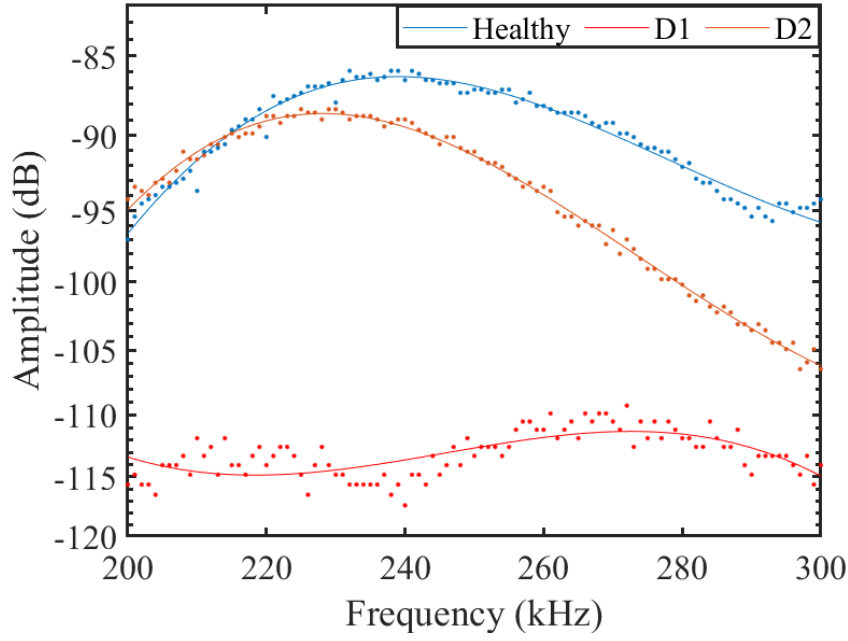


**Figure 10:** Comparing amplitude response curves to understand the influence of the impedance mismatch on the amplitudes of the symmetrically delaminated D1 and asymmetrically delaminated D2 signals across the frequency range determined in figure 6.

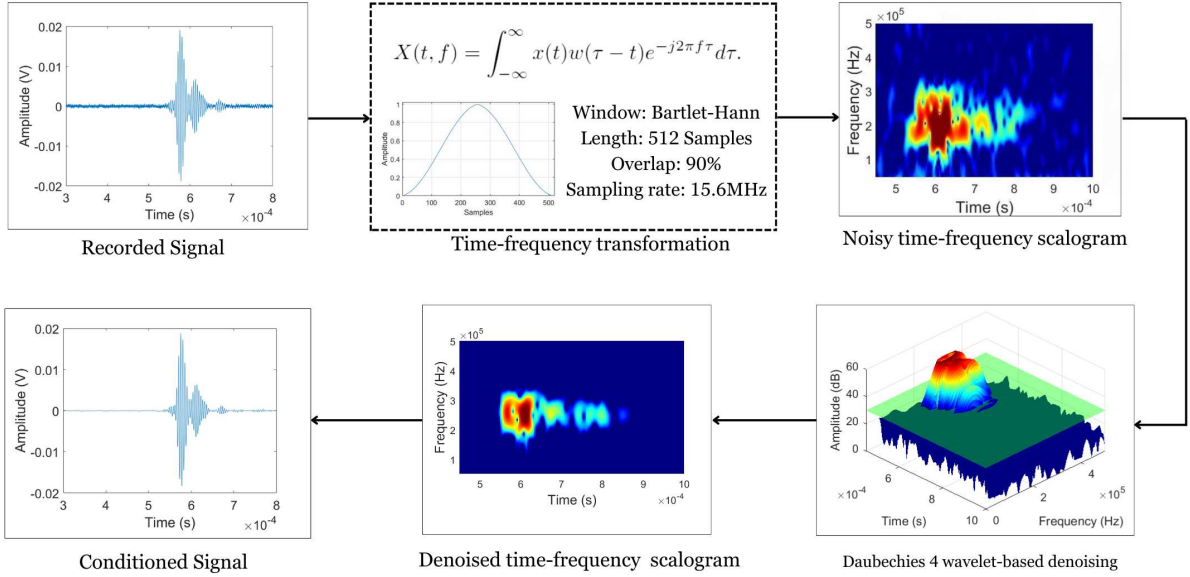


**Figure 11:** Conditioning and transformation of the raw acousto-ultrasonic signals into normalised time-frequency scalograms.

### 4.3 Signal conditioning and time-frequency transformations

An STFT provides a time-frequency representation of a signal by computing the Fourier Transform over short, overlapping time windows. This allows for the analysis of frequency content variations over time, revealing dynamic-changes in the signal characteristics. The time-frequency representations are also known as scalograms. These scalogram images can be used as input data to train machine learning algorithms that can accurately classify multiple damage

cases provided an optimum image resolution is maintained. It is worth noting that the machine learning aspect of this research will be explored in further detail in future studies. Mathematically, the STFT of a signal  $x(t)$  is obtained by multiplying the signal with a window function  $w(t)$  and applying the Fourier transform to each windowed segment. The window function helps to mitigate spectral leakage and reduce any noise introduced by sharp transitions at the edges of the window. The STFT of  $x(t)$  at a specific time  $t$  and frequency  $f$  is given by

$$X(t, f) = \int_{-\infty}^{\infty} x(\tau)w(\tau - t)e^{-j2\pi f\tau}d\tau. \quad (1)$$

where  $X(t, f)$  represents the STFT coefficients at time  $t$  and frequency  $f$ ,  $x(t)$  is the continuous time input signal,  $w$  is the window function and  $e^{-j2\pi f\tau}$  represents the complex exponential term where  $\tau$  is the time lag parameter. In practice, the discrete time Fourier transform (DTFT) of the  $m^{th}$  windowed block of the discrete-time signal  $x(n)$  for  $n = 0, 1 \dots N - 1$  where  $N$  is the window length is given by

$$X(m, w) = \text{DTFT} [x(n).w(n - m.N/2)] \quad (2)$$

The Bartlett-Hanning window was chosen for its balanced trade-off between spectral resolution and sidelobe suppression. This feature helps to reduce spectral leakage and minimize interference between frequency components.

$$\hat{X} = |X| \text{sgn}(|X| - X_{Threshold}) \quad \text{where} \quad \text{sgn}(X) = \begin{cases} 0 & \forall X \leq 0, \\ 1 & \forall X > 0. \end{cases} \quad (3)$$

In [equation 3](#),  $\hat{X}$  is the conditioned time-frequency scalogram. The signal conditioning entails denoising the acquired signals using a Daubechies 4 wavelet based algorithm. The denoising function estimates the standard deviation of the signal, establishes a threshold based on this estimation, and applies soft thresholding to attenuate the wavelet coefficients below the established threshold. This process effectively eliminates noise while retaining significant signal features.

$$\hat{x}(t) = \text{DTFT}^{-1} [\hat{X}(m, w)] \quad (4)$$

Upon performing an inverse STFT on  $\hat{X}$ , we obtain  $\hat{x}(t)$  which is the conditioned time-history waveform. This approach ensures that the denoised signal maintains its essential characteristics while minimizing unwanted noise, contributing to a clearer and more accurate representation of the original signal. The STFTs were generated with user-defined window length, overlap, frequency range and sampling rate. The resulting STFT plots represent the amplitude in decibels (dB) as a function of time and frequency, providing a comprehensive visual representation of the signal's time-varying frequency content.

When using STFT, the amplitude indicates the energy distribution of the incoming acoustic signals across the time-frequency scale. It helps to highlight the distribution of energy in the dominant propagating waves modes of the acousto-ultrasonic signal. To understand the influence of delaminations on the STFTs and establish concrete damage signatures, comparisons were made with the pristine baseline. The Bartlett-Hanning window with a window length of 512 samples (about 30% of total signal length of 16384 samples) and a 90% overlap between consecutive segments was selected to obtain clear time-frequency STFT scalograms. The frequency range of interest was set from 50kHz to 500kHz, covering the relevant frequency components. The resulting STFT plots provided detailed visualisations of the signal's frequency

content over time, facilitating the identification of specific frequency components and their temporal variations.

Building upon the observations from the time-history waveform analysis in [section 4.1](#), the STFTs were in agreement with the findings. In the amplitude vs time representation, the STFTs of D2 exhibited only a minor attenuation in the frequency content peaks, with the maximum peak occurring at a similar timestamp as the healthy STFT. Conversely, the symmetric D1 STFT showed a significant loss of frequency content accompanied by a shift of the maximum frequency content peak as seen in [figure 12](#).

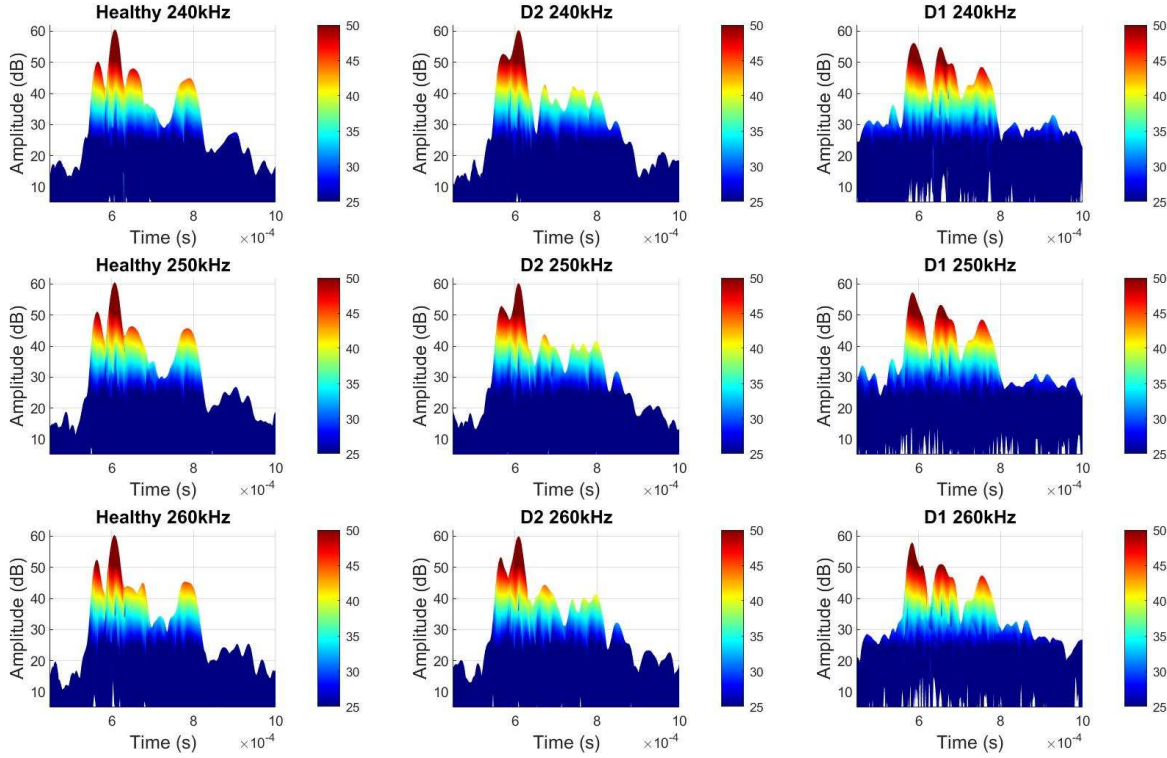


**Figure 12:** Time-Amplitude STFT representation of healthy, symmetric D1 and asymmetric D2 signals at 240kHz, 250kHz and 260kHz.

The features observed in the D2 scalograms suggest that the frequency components originally present in the pristine panel were largely retained, occurring at similar timestamps. On the other hand, the D1 STFT displayed a drop in amplitude and a maximum frequency content peak shift, suggesting that certain frequency components present in the pristine panel were not retained in the D1 region. These observations again align with the concept of impedance mismatch between the pristine and delaminated regions of the material. The changes in signal characteristics observed in D2 were minor due to a relatively lower impedance mismatch, whereas the changes in D1 were more pronounced due to a higher impedance mismatch. All the time-frequency scalograms shown in [figure 13](#) exhibited the highest energy between  $500\mu\text{s}$ – $700\mu\text{s}$ . However, the pristine scalogram revealed the highest energy amongst the three in that duration. In D2, the retained energy level was relatively lower than in the pristine case. In contrast, the D1 scalograms exhibited a significant loss of energy, indicative of the higher impedance mismatch introduced by D1. Similar to their time-history counterparts, the signal features of D1 are the closest to the noise floor. These results are consistent with the amplitude attenuation characteristics outlined in the previous sections.

The STFT results effectively captured the effects of delamination on the panel's signal char-



acteristics. The detailed time-frequency visualisation provided by the STFT analysis offered valuable insights into the frequency content variations over time. These findings laid the foundation for the subsequent analysis of the time of arrival of the first mode and the incorporation of uncertainty quantification, which will further enhance our understanding of the panel's structural health.

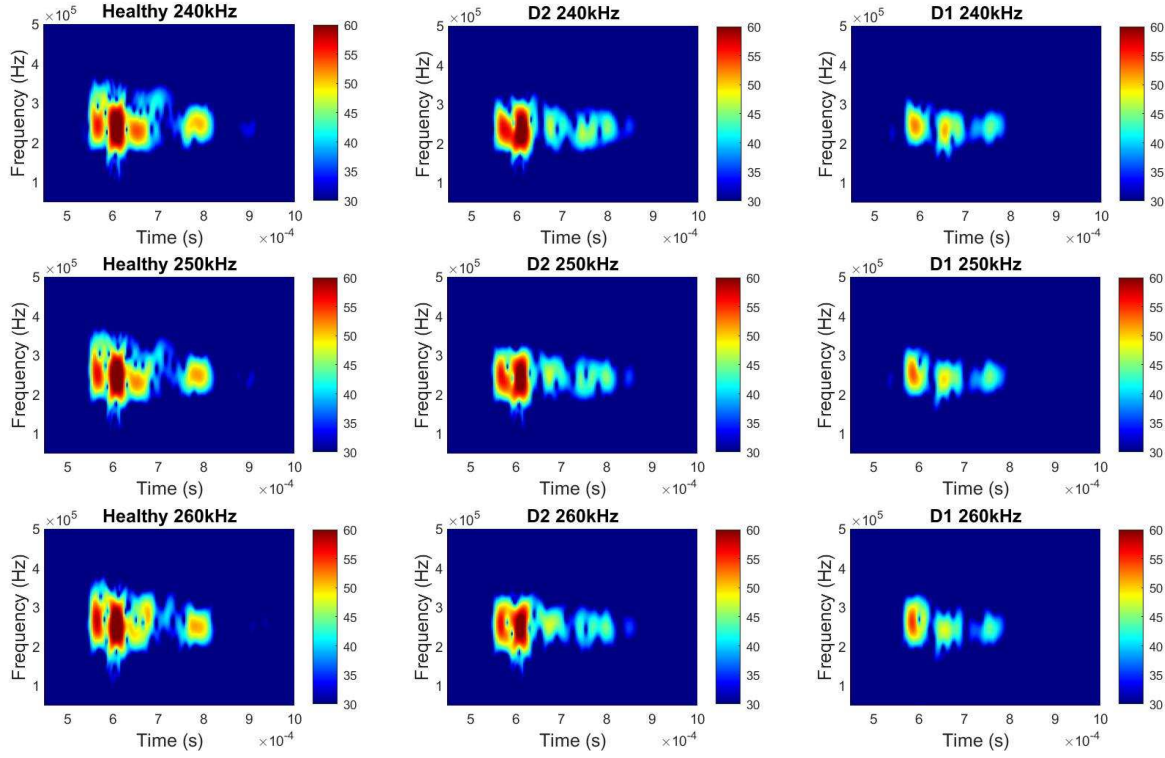


**Figure 13:** Time-frequency scalograms of healthy, asymmetric D2 and symmetric D1 signals at 240kHz, 250kHz and 260kHz generated using the methodology outlined in [figure 11](#).

#### 4.4 In-line signal classification on-the-edge

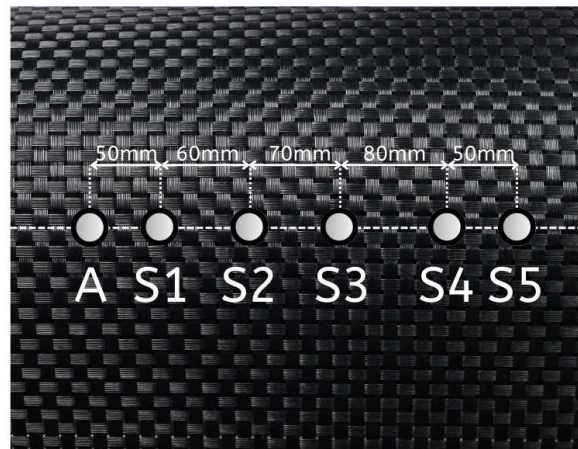


**Figure 14:** Linear array of actuator  $A$  and five transducers  $S_1 - S_5$  used to acquire data for in-line signal classification on-the-edge

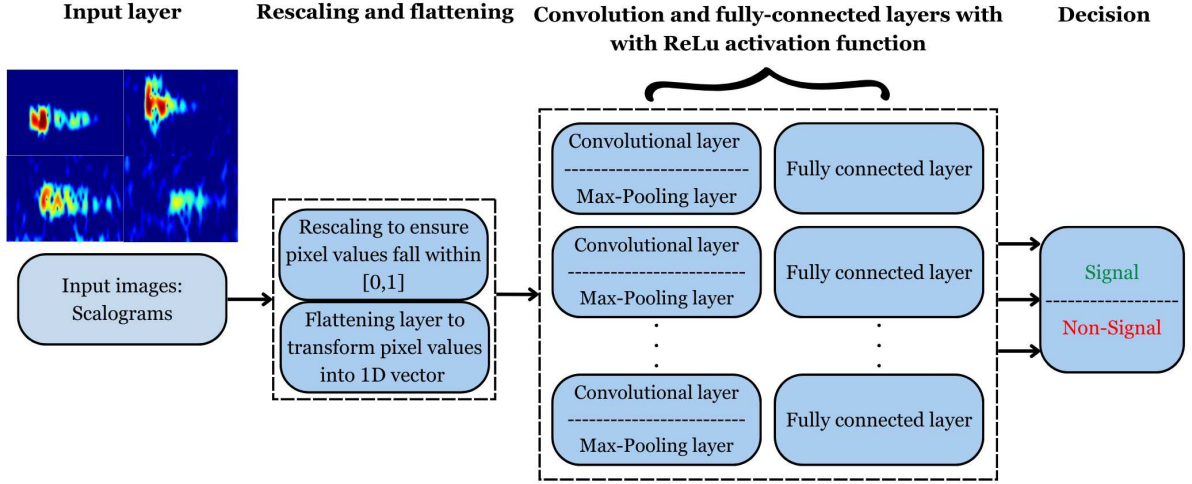


**Figure 15:** Flowchart of the employed classification algorithm operating on the edge device to distinguish between signals and non-signals.

The scalograms shown in [figure 13](#) are suitable as inputs to advanced image-based classification approaches, with a focus on distinguishing between various damage scenarios. However, the application in this context is designed to categorize the scalograms into two distinct classes – *AER* signals and *non- AER* signals. The developed classification algorithm was evaluated for its performance on the data obtained from a linear array of transducers  $S_1 - S_5$ , situated at varying distances from the actuator  $A$  shown in [figure 14](#). The pristine sample was actuated with a five cycle sinusoidal toneburst signal over a frequency band of 100 – 400kHz. The transducer array and the actuation frequency band were strategically chosen to encompass test scenarios with high signal to noise ratios (SNR) in  $S_1 - S_2$  and both low SNR and non-AER signal scenarios in  $S_3, S_4$  and  $S_5$ . The training data set included 300 scalograms from  $S_1$  and 15 scalograms from  $S_5$  to inform the algorithm of the spatial features of an AER signal and 300 scalograms of signals recorded with the input ports disconnected from transducers to inform the algorithm of the spatial features of a non-AER signal. The process flow of the algorithm is shown in [figure 15](#). 80% of the scalograms were allocated to train the model while the remaining 20% were used for validation according to the standardised approach outlined in [18]. The input layer holds the pixel values of the scalogram. The model architecture begins with a rescaling layer, an essential pre-processing step, where the pixel values are normalized for consistent data handling. These normalised pixel values are flattened into a one-dimensional vector which enables seamless data transition into the convolutional and fully-connected layers. The three convolutional layers are responsible for learning the spatial features of the scalograms. After each convolutional layer, a max pooling layer is applied which reduces the spatial dimensions of the features and retains the most important information. The fully-connected layers produce class scores which are used for classification. ReLu was used between the layers to improve classifier performance [60].

The confusion matrix shown in [figure 16](#) encapsulates the performance of the classifier. With a total of 1505 images , in consideration as test data set, the model accurately classified the instances 92.56% of the time. The misclassification rate, reflecting the proportion of erroneous predictions, stands at 7.44%, representing the model’s margin of error. The true positivity rate underscores its ability to correctly identify signals when they are genuinely present, achieving a rate of 98.44%. Notably, the true negativity rate indicating how often the model classifies the data as non-AER signals when in fact they are non-AER signals, is 67.93%. Identifying

data files with undesirable non-signals is critical for purging, ensuring only essential data files are relayed to the digital layer for further analysis and characterization. Figure 17 provides insights into the algorithm's confidence levels at distinct frequency points. In this visualisation, accurate signal predictions are denoted by blue circles, accurate non-signal predictions by blue  $\times$ 's and erroneous predictions by red circles. The opacity of the blue circles indicates prediction confidence, with decreasing opacity representing lower confidence. Observations reveal accurate classifications for signals from  $S_1$  (50mm from the actuator) and  $S_2$  (110mm from the actuator) which contained signals with high signal to noise ratios. Data obtained from  $S_3$  (180mm from the actuator) comprised of both signals and non-signals(100kHz-160kHz) which were classified with 96.01% accuracy. Signals and non-signals from  $S_4$  (260mm from the actuator) and  $S_5$  ((310mm from the actuator) were accurately classified 89.70% and 79.06% of the time, respectively. The erroneous predictions were concentrated at frequencies above 350kHz. The overall classification accuracy of the algorithm is 92.55%.

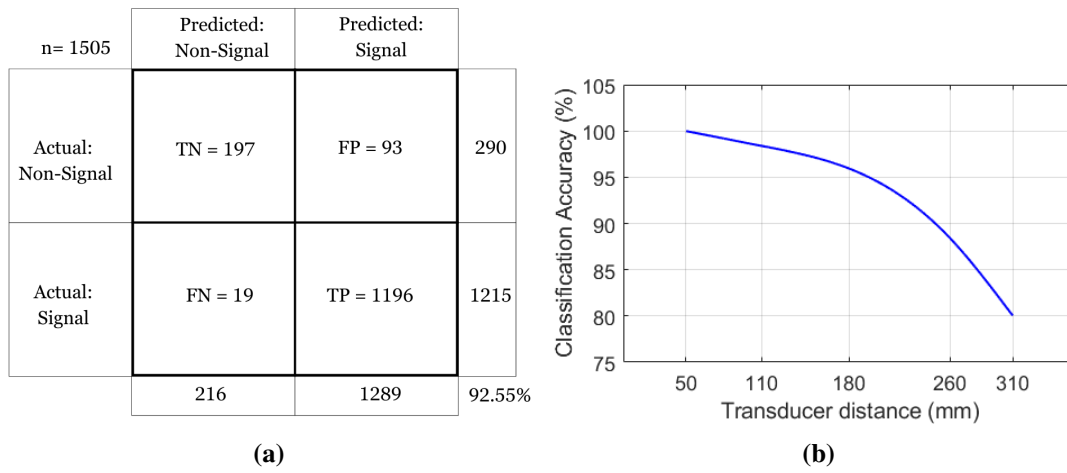


**Figure 16:** (a) Confusion matrix to depict CNN algorithm's performance in distinguishing between AER signal and non-AER signal in a test data set of 1505 files. (TN-True Negative, TP-True Positive, FN-False Negative, FP-False Positive) and (b) classification accuracy of the algorithm as a function of transducer distance

In summary, a classification algorithm was developed to categorise acquired data into essential acoustic event representative signals and non-essential signals on-the-edge. Its performance could be further enhanced by increasing the energy of the actuation signal, improving the coupling between the transducer and the sample or subjecting the recorded signals to additional pre-conditioning tasks, specifically focused on refining their frequency content.

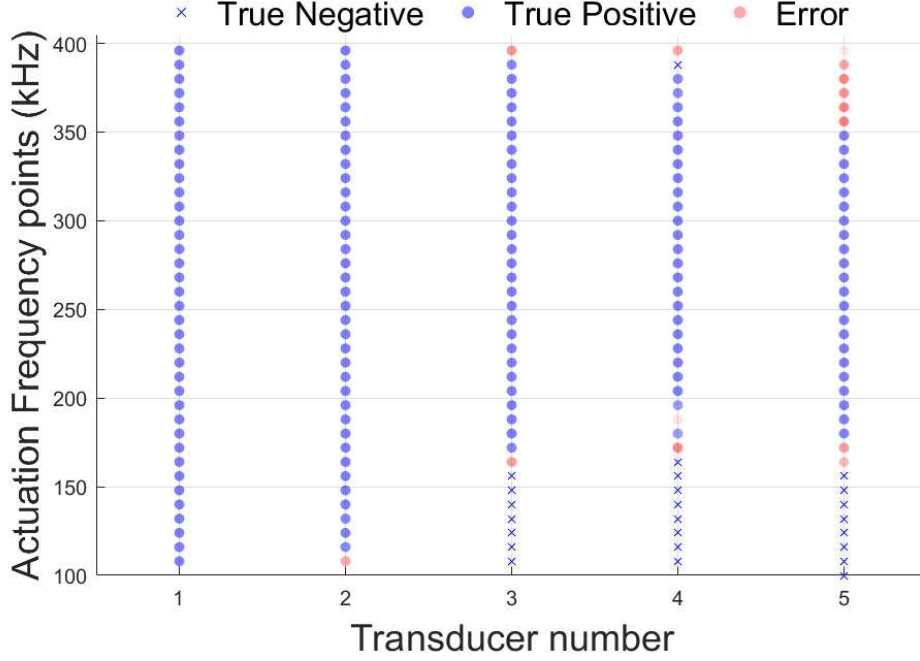


**Figure 17:** Varying levels of marker opacity representing the classifier prediction confidence of signals obtained at each sensor  $S_1 - S_5$  across discrete 1kHz actuation frequency points from 100 – 400kHz.

#### 4.5 Wave velocity calculation and uncertainty quantification

Monitoring the time of arrival of the first mode provides valuable insights into the identification fundamental UGW modes and eventually the damage signatures that describe structural integrity and health of a component. In a pristine panel, UGW modes occur based on material properties and the nature of their interactions with the material. The pristine modes serve as a baseline reference for the component’s undamaged state. However, in presence of a damage, the behavior of UGW modes is altered. The damage causes a significant portion of the propagating signal to be reflected or scattered away with only a fraction of it being transmitted to the transducers where they are recorded. These changes in velocity and arrival time can be indicative of the presence of damage such as cracks, delaminations or material degradation. The location of the damage can be determined using measurements of the time of arrival (TOA) at a certain sensor and time difference of arrival (TDOA) of the signals detected at various sensors [61]. Using TOA, one can also determine the propagating wave velocity ( $V_p$ ). Errors in estimating the location of the damage can stem from miscalculations made in determining either of these parameters. Therefore, it is important to maximise the accuracy with which the point of signal onset is determined. [62]

In this study, the time of arrival of first mode is estimated based on the Akaike Information Criterion (AIC) [63]. The AIC is a statistical measure commonly used for model selection and hypothesis testing. It provides a way to compare different models and determine the one that best describes the data at hand. The fundamental idea behind AIC is to balance the goodness of fit of a model with its complexity. When applied to time series analysis or signal processing, AIC can be used to estimate the point where a coherent signal emerges from background noise. This is particularly useful in scenarios where the onset of a specific event or phenomenon in a time series signal needs to be identified [64]. In the current case, AIC was utilized for signal onset detection where the time-series signal was divided into two sections at a given point  $t$

within a time window. The criterion for choosing this time window is based on trial and error. The same window size of 512 samples was used to maintain consistency in the calculations. The AIC is then calculated based on the statistical variances of the left and right sections. The AIC value [65] is calculated using the expression

$$\text{AIC}(t) = t \log(\text{Var}[x[1:t]]) + (N - t - 1) \log(\text{Var}[x[t:N]]) \quad (5)$$

where,  $t$  is the transition point within the time window,  $N$  is the length of the time window,  $\text{Var}[x[1:t]]$  is the variance of the left section of the signal and  $\text{Var}[x[t:N]]$  is the variance of the right section of the signal. By iterating over different points of division within the

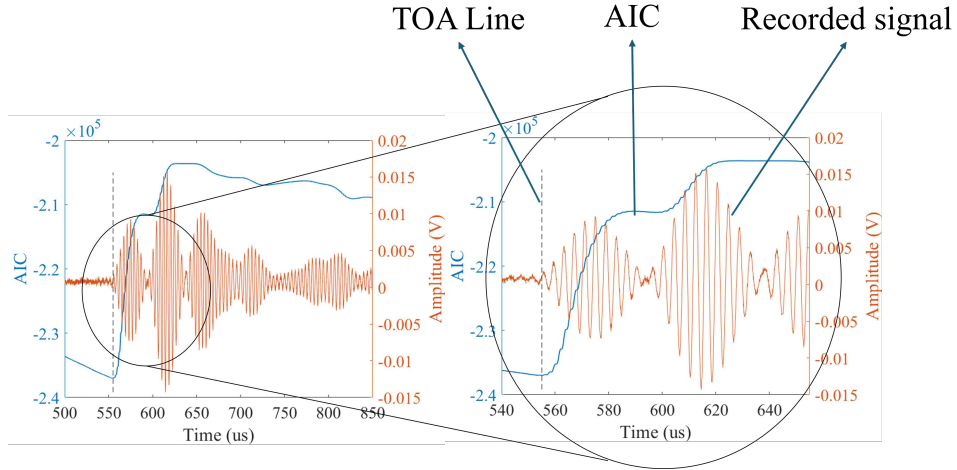


**Figure 18:** Estimating the point of signal onset using the information criterion (AIC) criterion outlined in [equation 5](#). This provides more robust estimates of the time-of-arrival compared to threshold based onset estimations, especially for closely spaced overlapping or acoustic events and poor SNR signals.

time window and selecting the one with the minimum AIC value, the point of signal onset is identified. Intuitively, it can be understood that the AIC-provided transition point between noise and signals will likely exhibit a significant change in variance. This approach allows a statistical analysis of the signal to determine the most likely location where the coherent signal emerges from background noise as observed in [figure 18](#).

In [figure 19](#), distinct time of arrival and wave velocity characteristics can be observed for the three cases of the pristine, symmetrically delaminated and asymmetrically delaminated panels. Specifically, the D1 signal exhibits the earliest time of arrival of first mode, which is indicative of a high impedance mismatch. Because a significant portion of the signal is reflected away, the energy of the wave modes propagating through D1 experiences substantial attenuation and hence arrives at the transducer with a noticeable delay. On the other hand, both pristine and D2 signals demonstrate similar time of arrival and wave velocity characteristics, with the pristine mode arriving the earliest amongst the three cases. This finding suggests that the pristine signal experiences a relatively minimal energy loss during propagation. The similarity in the time of arrival and wave velocity characteristics between the pristine and D2 signals suggests a lower impedance mismatch for D2. Although D2 still exhibits some energy loss during propagation, it is less pronounced compared to D1. This means that the structural changes induced by the presence of D2 result in a relatively smaller deviation from the surrounding medium, leading to a lesser degree of energy loss and a closer resemblance to the pristine signal's time of arrival characteristics as explained in [section 4.1](#).



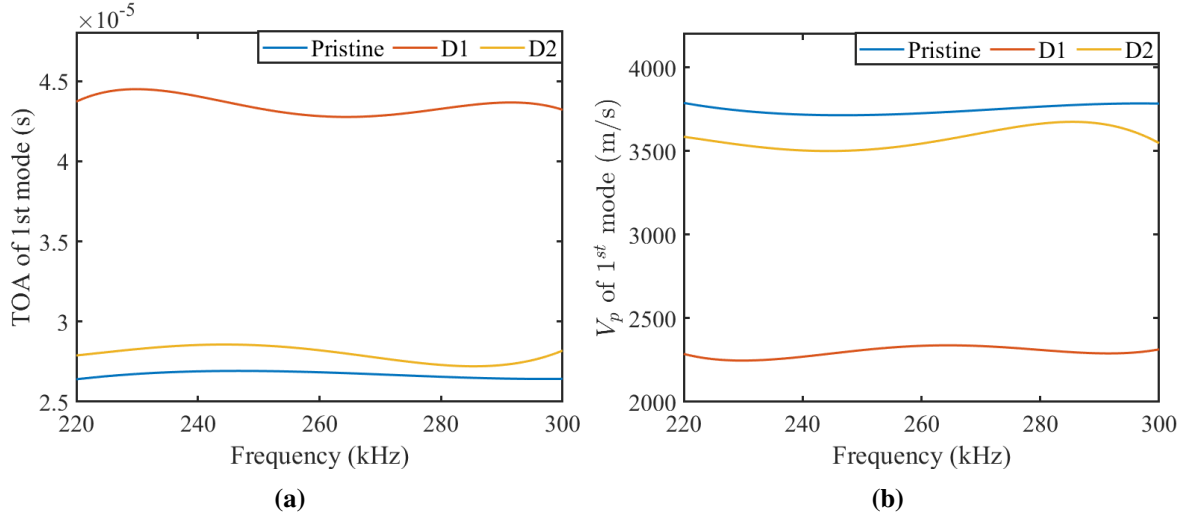


**Figure 19:** (a) Time of arrival and (b) propagating wave velocity of the earliest arriving ultrasonic guided wave mode in the pristine, symmetric D1 and asymmetric D2 signals.

Considering the time of arrival of the incoming wavefront/first mode  $t$  and the distance between the transducers  $d$ , the propagating wave velocity of the first mode was calculated. Quantifying the uncertainty associated with  $t$  and  $d$  is a key component of this analysis. The uncertainties for distance  $d$  and arrival time  $t$  in terms of mean distance  $d_0$  and time of arrival  $t_0$  are expressed as

$$d = d_0 + \varepsilon_d \quad \text{and} \quad t = t_0 + \varepsilon_t \quad (6)$$

where,

1.  $\varepsilon_d$  and  $\varepsilon_t$  are zero-mean Gaussian noise representing the uncertainty of the measured sensor-actuator distance and the time of arrival of the acousto-ultrasonic signal at the sensors respectively, hence

$$\varepsilon_d \sim \mathcal{N}(0, \sigma_d^2) \quad \text{and} \quad \varepsilon_t \sim \mathcal{N}(0, \sigma_t^2) \quad (7)$$

2. the uncertainties  $\varepsilon_d$  and  $\varepsilon_t$  are independent of each other.
3. the uncertainties in  $\varepsilon_d$  and  $\varepsilon_t$  are much smaller than the actual scales of  $d$  and  $t$ , which implies  $\frac{\varepsilon_d}{d_0} \ll 1$  and  $\frac{\varepsilon_t}{t_0} \ll 1$ .

The wave velocity  $u$  is represented as

$$u = u_0 + \varepsilon_u \quad \text{where} \quad \varepsilon_u \sim \mathcal{N}(0, \sigma_u^2) \quad (8)$$

such that we assume the uncertainty in  $u$  as a zero-mean Gaussian noise  $\varepsilon_u$ . The mean velocity  $u_0$  and the associated variance expressed as  $\sigma_u^2$  are calculated below.

$$u_0 = \mathbb{E} \left[ \frac{d_0 + \varepsilon_d}{t_0 + \varepsilon_t} \right] = \frac{d_0}{t_0} \mathbb{E} \left[ \frac{1 + \frac{\varepsilon_d}{d_0}}{1 + \frac{\varepsilon_t}{t_0}} \right] = \frac{d_0}{t_0} \mathbb{E} \left[ \left( 1 + \frac{\varepsilon_d}{d_0} \right) \left( 1 + \frac{\varepsilon_t}{t_0} \right)^{-1} \right] \quad (9)$$

Noting  $\frac{\varepsilon_t}{t_0} \ll 1$ , [equation 9](#) can be represented as a convergent binomial series

$$\begin{aligned} u_0 &= \frac{d_0}{t_0} \mathbb{E} \left[ \left( 1 + \frac{\varepsilon_d}{d_0} \right) \left( 1 - \frac{\varepsilon_t}{t_0} + \left( \frac{\varepsilon_t}{t_0} \right)^2 - \left( \frac{\varepsilon_t}{t_0} \right)^3 + \dots \right) \right] \\ &\approx \frac{d_0}{t_0} \mathbb{E} \left[ \left( 1 + \frac{\varepsilon_d}{d_0} \right) \left( 1 - \frac{\varepsilon_t}{t_0} \right) \right] \end{aligned} \quad (10)$$

where the higher order terms have been neglected. Hence,

$$\begin{aligned} u_0 &= \frac{d_0}{t_0} \mathbb{E} \left[ 1 - \frac{\varepsilon_t}{t_0} + \frac{\varepsilon_d}{d_0} - \frac{\varepsilon_d \varepsilon_t}{d_0 t_0} \right] \\ &= \frac{d_0}{t_0} \left[ 1 - \mathbb{E} \left[ \frac{\varepsilon_t}{t_0} \right] + \mathbb{E} \left[ \frac{\varepsilon_d}{d_0} \right] - \mathbb{E} \left[ \frac{\varepsilon_t \varepsilon_d}{t_0 d_0} \right] \right] \end{aligned} \quad (11)$$

Since  $\varepsilon_d$  and  $\varepsilon_t$  are independent of each other and are zero-mean noises as mentioned in argument [1](#), we have

$$u_0 = \frac{d_0}{t_0} \quad (12)$$

Hence under the assumption of relatively small uncertainty, the mean velocity of acousto-ultrasonic wavefront is simply the ratio of the mean actuator-sensor distance and the mean time-of arrival. The variance of velocity  $u$  can be calculated as function of the uncertainty in the measured time of arrival  $\varepsilon_t$  and wave travel distance  $\varepsilon_d$  as

$$\sigma_u^2 = \mathbb{E} (u^2) - [\mathbb{E} (u)]^2 = \mathbb{E} (u^2) - u_0^2 \quad (13)$$

Hence following a similar treatment of the equations as in [equation 9](#)

$$\begin{aligned} \sigma_u^2 &= \mathbb{E} \left[ \left( \frac{d_0 + \varepsilon_d}{t_0 + \varepsilon_t} \right)^2 \right] = \left( \frac{d_0}{t_0} \right)^2 \mathbb{E} \left[ \left( \frac{1 + \frac{\varepsilon_d}{d_0}}{1 + \frac{\varepsilon_t}{t_0}} \right)^2 \right] \\ &= u_0^2 \mathbb{E} \left[ \left( 1 + \frac{\varepsilon_d}{d_0} \right)^2 \left( 1 + \frac{\varepsilon_t}{t_0} \right)^{-2} \right] \end{aligned} \quad (14)$$

$$\sigma_u^2 = u_0^2 \mathbb{E} \left[ \left( \left( 1 + \frac{\varepsilon_d}{d_0} \right)^2 \right) \left( 1 - 2 \left( \frac{\varepsilon_t}{t_0} \right) + 3 \left( \frac{\varepsilon_t}{t_0} \right)^2 - 4 \left( \frac{\varepsilon_t}{t_0} \right)^3 + \dots \right) \right] \quad (15)$$

Again, following argument [3](#), the higher order terms may be neglected.

$$\sigma_u^2 \approx u_0^2 \mathbb{E} \left[ \left( 1 + 2 \frac{\varepsilon_d}{d_0} + \left( \frac{\varepsilon_d}{d_0} \right)^2 \right) \left( 1 - 2 \frac{\varepsilon_t}{t_0} + 3 \left( \frac{\varepsilon_t}{t_0} \right)^2 \right) \right] \quad (16)$$

Since the noise  $\varepsilon_d$  and  $\varepsilon_t$  are independent as per argument [2](#), the  $\mathbb{E}$  operator may be applied as follows

$$\sigma_u^2 = u_0^2 \mathbb{E} \left[ 1 + 2 \frac{\varepsilon_d}{d_0} + \left( \frac{\varepsilon_d}{d_0} \right)^2 \right] \mathbb{E} \left[ 1 - 2 \frac{\varepsilon_t}{t_0} + 3 \left( \frac{\varepsilon_t}{t_0} \right)^2 \right] \quad (17)$$

Following argument [1](#)

$$\sigma_u^2 = u_0^2 + 3u_0^2 \mathbb{E} \left[ \left( \frac{\varepsilon_t}{t_0} \right)^2 \right] + u_0^2 \mathbb{E} \left[ \left( \frac{\varepsilon_d}{d_0} \right)^2 \right] + 3u_0^2 \mathbb{E} \left[ \left( \frac{\varepsilon_d}{d_0} \right)^2 \right] \mathbb{E} \left[ \left( \frac{\varepsilon_t}{t_0} \right)^2 \right]$$

$$\frac{\sigma_u^2}{u_0^2} \approx 1 + V(\varepsilon_d) + 3V(\varepsilon_t) \quad (18)$$

The contributions of the uncertainty associated with the actuator-sensor distance and the time of arrival of the first mode can be inferred from [equation 18](#) where  $V(\varepsilon_d)$  and  $V(\varepsilon_t)$  denote the mean normalized variances of  $\varepsilon_d$  and  $\varepsilon_t$ . The uncertainty associated with  $\varepsilon_t$  is at least three times that of  $\varepsilon_d$ . This aligns with the meticulous transducer placement conducted with accurate measurements, thereby leaving scope for minor human errors in  $d$ . On the other hand, the time of arrival  $t$  was calculated based on a statistical criterion that distinguishes signal from noise, which is prone to a higher degree of uncertainty. The calculated wave velocities along with their corresponding confidence bounds are plotted against frequency-thickness product in [figure 20](#). In case of D1, which showed a delayed arrival in the time-history waveforms, significant amplitude attenuation in the amplitude response curves and the shortest sustained duration in the time-frequency scalograms (STFTs), the wave velocity was found to be the lowest among all the cases. These observations suggest a significant loss of energy, which can be attributed to a high impedance mismatch.

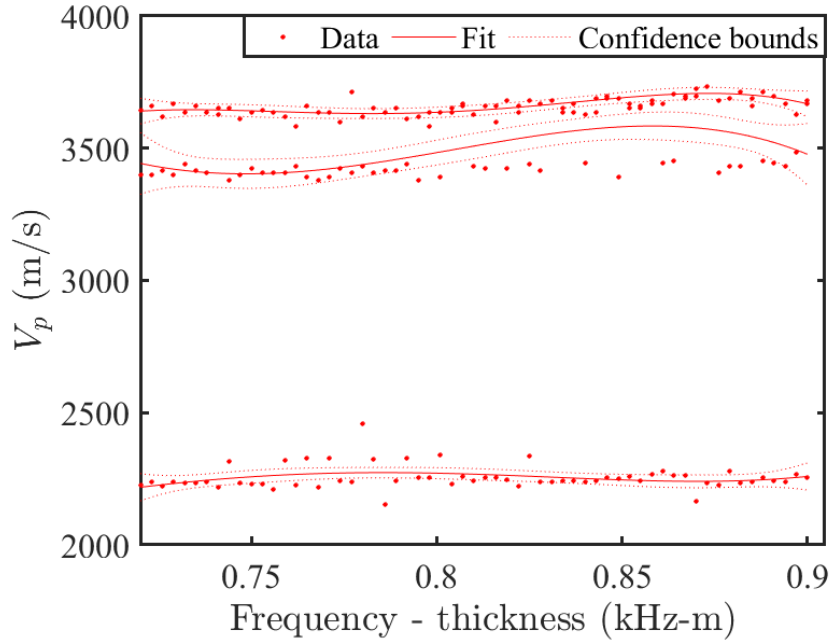


**Figure 20:** Wave velocity  $V_p$  with 99% confidence bounds for estimating the earliest arriving ultrasonic guided wave mode in pristine, asymmetric D2, and symmetric D1 waveguides.

On the other hand, in case of D2, which exhibited a relatively low time delay in the time-history waveforms, minor amplitude attenuation in the amplitude response analysis and a sustained duration close to but smaller than the pristine case, the wave velocity was higher than D1 but 16.67% lower than the pristine case. This indicates a relatively lower impedance mismatch and loss of energy. The analysis of propagating wave velocities not only sheds light on the recorded wave modes in the experiments but also serves as a crucial starting point for calculating slowness curves.

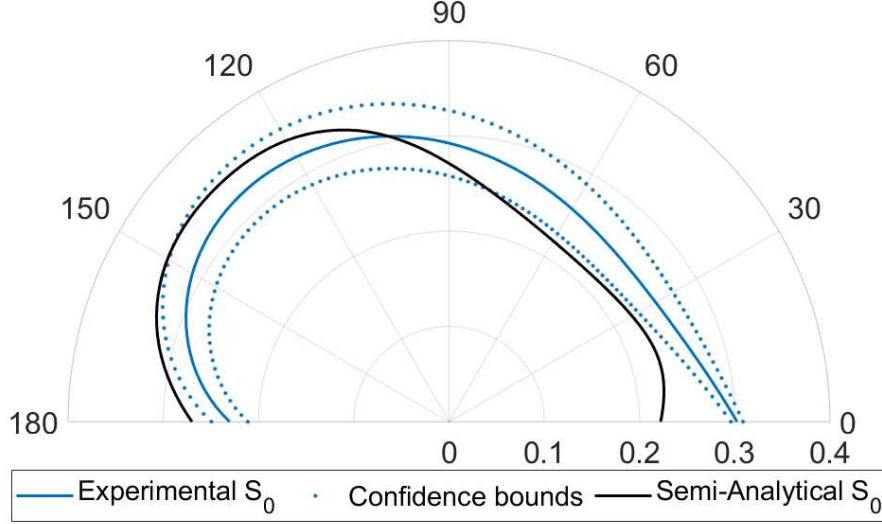


**Figure 21:** Comparing the shapes of the experimental slowness curve with 99% confidence bounds and Semi Analytical Finite Element  $S_0$  slowness curve of the pristine sample for wave mode identification.

#### 4.6 Slowness curves and wave mode identification

In ultrasonic guided wave testing, slowness curves play a vital role in wave mode identification. The wave slowness is the inverse of the wave velocity and represents how quickly the wave propagates through the composite panel in different directions. By examining the shape and behavior of the slowness curve, one can identify different wave modes. Each wave mode has a distinctive polar map of slowness as a function of the ply orientation and elastic properties, thereby enabling the isolation and identification of symmetric, antisymmetric modes of different orders. In this study, a semi-circular array configuration of the transducers (figure 7) allowed for the analysis of wave velocities along multiple directions. The point of signal onset was identified using the AIC criterion and the time of arrival was computed using this point. This in turn lead to the calculation of the wave velocity and the slowness of the earliest arriving mode. The calculated slowness values were plotted against propagation angles  $0, \frac{\pi}{4}, \frac{\pi}{2}, \frac{3\pi}{4}$  and  $\pi$ . The slowness curve of the earliest arriving mode generated using experimental data was compared against the curves generated by the semi-analytical method as shown in figure 21. The recorded wave mode was determined to be the symmetric  $S_0$  mode. More information on wave mode interactions with composite structures can be found in [66]–[68].

The analysis of time-history waveforms, amplitude responses and STFTs yields valuable insights into the impact of delaminations on the ultrasonic guided wave signals. The location of the delamination relative to the central axis of the panel plays a crucial role in determining the degree of amplitude attenuation and frequency content changes in the signals. The observed amplitude attenuation effects of signals in time domain were not only consistent when examined in the frequency domain but also complimented by their time-frequency representations. Delayed signal arrival in the time-history waveforms, distinct amplitude attenuation characteristics in the amplitude response analysis, reduced signal energies in the time-frequency representations and the calculated wave velocities were identified as reliable damage signatures. It is worth noting that the entire workflow, starting from signal acquisition to signal post processing and analysis including detecting and classification of damages, was efficiently performed using the edge device. The various signal post processing techniques employed in this study

are summarised in [figure 22](#).

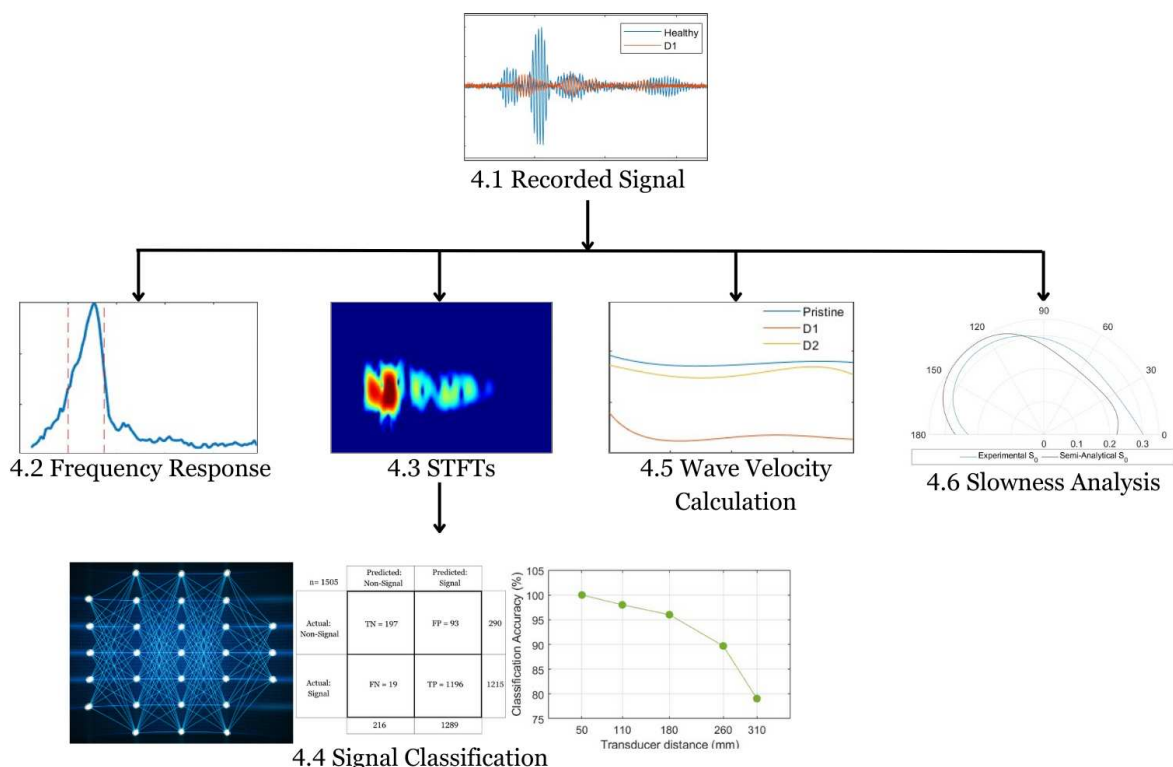


**Figure 22:** Signal postprocessing techniques applied to the acquired ultrasonic guided wave signals followed by acoustic source classification.

The proposed workflow, encompassing the detection and classification of signals based on the identified damage signatures, marks a crucial step towards realising an autonomous and intelligent CPS in the field of SHM. By successfully integrating signal processing techniques and edge computing capabilities, this study demonstrated the feasibility of performing complex SHM tasks efficiently and autonomously. The established workflow offers reduced lead times and highlights the potential of utilizing the physical layer of CyberSHM to detect and classify various types of damages. It is important to note that the signal acquisition, classification, and processing capabilities demonstrated by the CyberSHM physical layer in this study represent a crucial initial step towards the realization of a non-intrusive autonomous Structural Health Monitoring (SHM) system. Future research will focus on leveraging the established framework to effectively isolate fundamental ultrasonic guided wave modes and investigate the changes in their modal properties as a function of introduced damage. Mapping these changes to parameterized damage metrics will help establish reliable damage signatures, providing engineers with detailed information about the current health state of the structure and enabling the determination of optimal maintenance intervention points. This enhanced understanding will facilitate the development of a physics-informed, robust, and non-intrusive SHM system with real-time decision-making capabilities.

## 5 Conclusions

This study presents a comprehensive analysis and development of a CPS physical layer, integrating threshold-free on-edge damage detection and classification capabilities within the Cy-



berSHM framework. The physical layer operated through two parallelly running algorithms—the interrogation algorithm and the file-check algorithm. The interrogation algorithm excited the structure of interest with a user-defined signal via a sparse array of transducers and saved the acquired data on the edge device. Triggered by the onset of a new batch of data, an in-line classification algorithm, known as the file-check algorithm classified the acquired data into AER or non-AER signals. Non-AER signal data was eliminated from the edge device while the AER signal was subjected to feature extraction algorithms.

The experimental validation of the physical layer was conducted on a  $(500 \times 500 \times 3)$  mm 12-layer  $[+45_3 / -45_3]_S$  CFRC panel with symmetric D1 and asymmetric D2  $(30 \times 30 \times 0.02)$  mm delaminations. The recorded signals were investigated in time, frequency and frequency-time domains using a time-history waveform study, amplitude response curves, STFTs, TOA and slowness curve analysis where the pristine panel was differentiated from the damaged panel and both the damage cases were distinguished. Furthermore, the AIC criterion was used to determine the TOA, velocity and slowness of the earliest arriving mode. The uncertainties associated with distance between the transducers and the time of arrival were incorporated into the wave velocity calculations, quantifying the overall uncertainty in the wave velocity. The determination of the velocity not only aided in differentiating the damaged composite panel from the pristine panel, but also between the damaged cases. Furthermore, the symmetric  $S_0$  was identified as the earliest arriving mode with close resemblance between the experimental and semi-analytical slowness curve shapes.

The CyberSHM physical layer is not only envisioned to carry out real-time in-service data acquisition, damage detection and characterisation tasks but also to make intelligent projections and extrapolations upon exploring scenarios that the host structure is yet to encounter. In applications where large volumes of data are recorded, limited computing ability and sensor memory space is a significant challenge. It is of paramount importance that the essential features are extracted swiftly to facilitate efficient and well-informed decision-making. To this light, a compressive sensing framework can be employed wherein one can acquire sparse data and reconstruct the signal in such a way that the essential features embedded in the original signal are preserved in the process of compression and reconstruction. The developed workflow facilitated wireless access to the device. This is crucial in addressing deployment challenges in an autonomous CPS where the data collected by the physical layer can be relayed to a cloud-based server where various classification and simulation models can act on them. Future work will concentrate on robust disentanglement of the fundamental ultrasonic guided wave modes and investigate the changes in the content of each propagating mode as a function of damage introduced into the structure. This will lead to the estimation of damage signatures from acquired ultrasonic signals and inform the overall health metric of the structure.

## Funding Data

This research was funded by Engineering and Physical Sciences Research Council (EPSRC), UK under grant number EP/V055577/1.

## Declaration of competing interests

The authors declare that they have no known competing financial interests or personal relationships that could have appeared to influence the work reported in this paper.

## References

- [1] M. G. R. Sause and E. Jasiūnienė, Eds., *Structural Health Monitoring Damage Detection Systems for Aerospace* (Springer Aerospace Technology), en. Cham: Springer International Publishing, 2021, ISBN: 978-3-030-72191-6 978-3-030-72192-3. DOI: 10.1007/978-3-030-72192-3.
- [2] V. Arora, Y. Wijnant, and A. de Boer, “Acoustic-based damage detection method,” *Applied Acoustics*, vol. 80, pp. 23–27, 2014, ISSN: 0003-682X. DOI: <https://doi.org/10.1016/j.apacoust.2014.01.003>.
- [3] E. Verstryngne, G. Lacidogna, F. Accornero, and A. Tomor, “A review on acoustic emission monitoring for damage detection in masonry structures,” *Construction and Building Materials*, vol. 268, p. 121 089, 2021, ISSN: 0950-0618. DOI: <https://doi.org/10.1016/j.conbuildmat.2020.121089>.
- [4] M. Mitra and S. Gopalakrishnan, “Guided wave based structural health monitoring: A review,” *Smart Materials and Structures*, vol. 25, no. 5, p. 053 001, Mar. 2016. DOI: 10.1088/0964-1726/25/5/053001.
- [5] L. Capineri and A. Bulletti, “Ultrasonic Guided-Waves Sensors and Integrated Structural Health Monitoring Systems for Impact Detection and Localization: A Review,” en, *Sensors*, vol. 21, no. 9, p. 2929, Apr. 2021, ISSN: 1424-8220. DOI: 10.3390/s21092929.
- [6] S. Sawant, S. Banerjee, and S. Tallur, “Performance evaluation of compressive sensing based lost data recovery using OMP for damage index estimation in ultrasonic SHM,” en, *Ultrasonics*, vol. 115, p. 106 439, Aug. 2021, ISSN: 0041624X. DOI: 10.1016/j.ultras.2021.106439.
- [7] M. Jayawardhana, X. Zhu, R. Liyanapathirana, and U. Gunawardana, “Compressive sensing for efficient health monitoring and effective damage detection of structures,” en, *Mechanical Systems and Signal Processing*, vol. 84, pp. 414–430, Feb. 2017, ISSN: 08883270. DOI: 10.1016/j.ymssp.2016.07.027.
- [8] Y. Bao, H. Li, and J. Ou, “Emerging data technology in structural health monitoring: Compressive sensing technology,” en, *J Civil Struct Health Monit*, vol. 4, no. 2, pp. 77–90, Apr. 2014, ISSN: 2190-5452, 2190-5479. DOI: 10.1007/s13349-013-0064-1.
- [9] C. Zhang, A. A. Mousavi, S. F. Masri, G. Gholipour, K. Yan, and X. Li, “Vibration feature extraction using signal processing techniques for structural health monitoring: A review,” en, *Mechanical Systems and Signal Processing*, vol. 177, p. 109 175, Sep. 2022, ISSN: 08883270. DOI: 10.1016/j.ymssp.2022.109175.
- [10] M. E. Mountassir, S. Yaacoubi, J. Ragot, G. Mourot, and D. Maquin, “Feature selection techniques for identifying the most relevant damage indices in SHM using Guided Waves,” en,
- [11] I. Dafydd and Z. Sharif Khodaei, “Analysis of barely visible impact damage severity with ultrasonic guided Lamb waves,” en, *Structural Health Monitoring*, vol. 19, no. 4, pp. 1104–1122, Jul. 2020, ISSN: 1475-9217, 1741-3168. DOI: 10.1177/1475921719878850.

- [12] A. Gullapalli, V. Beedasy, J. D. S. Vincent, Z. Leong, P. Smith, and N. Morley, “Flat Inkjet-Printed Copper Induction Coils for Magnetostrictive Structural Health Monitoring: A Comparison with Bulk Air Coils and an anisotropic magnetoresistive sensor (AMR) Sensor,” en, *Adv Eng Mater*, vol. 23, no. 9, p. 2100313, Sep. 2021, ISSN: 1438-1656, 1527-2648. DOI: 10.1002/adem.202100313.
- [13] Z. H. Liu, Q. L. Peng, X. Li, C. F. He, and B. Wu, “Acoustic Emission Source Localization with Generalized Regression Neural Network Based on Time Difference Mapping Method,” en, *Exp Mech*, vol. 60, no. 5, pp. 679–694, Jun. 2020, ISSN: 0014-4851, 1741-2765. DOI: 10.1007/s11340-020-00591-8.
- [14] S. Sony, K. Dunphy, A. Sadhu, and M. Capretz, “A systematic review of convolutional neural network-based structural condition assessment techniques,” *Engineering Structures*, vol. 226, p. 111347, 2021, ISSN: 0141-0296. DOI: <https://doi.org/10.1016/j.engstruct.2020.111347>.
- [15] K. Chandrasekhar, N. Stevanovic, E. J. Cross, N. Dervilis, and K. Worden, “Gaussian Processes for Structural Health Monitoring of Wind Turbine Blades,” en, in *Structural Health Monitoring 2019*, DEStech Publications, Inc., Nov. 2019, ISBN: 978-1-60595-601-5. DOI: 10.12783/shm2019/32419.
- [16] I. Farreras-Alcover, M. K. Chryssanthopoulos, and J. E. Andersen, “Regression models for structural health monitoring of welded bridge joints based on temperature, traffic and strain measurements,” *Structural Health Monitoring*, vol. 14, no. 6, pp. 648–662, 2015. DOI: 10.1177/1475921715609801. eprint: <https://doi.org/10.1177/1475921715609801>.
- [17] A. Kundu, S. Sikdar, M. Eaton, and R. Navaratne, “A Generic Framework for Application of Machine Learning in Acoustic Emission-Based Damage Identification,” en, in *Proceedings of the 13th International Conference on Damage Assessment of Structures*, M. A. Wahab, Ed., Series Title: Lecture Notes in Mechanical Engineering, Singapore: Springer Singapore, 2020, pp. 244–262, ISBN: 9789811383304 9789811383311. DOI: 10.1007/978-981-13-8331-1\_18.
- [18] S. Sikdar, D. Liu, and A. Kundu, “Acoustic emission data based deep learning approach for classification and detection of damage-sources in a composite panel,” en, *Composites Part B: Engineering*, vol. 228, p. 109450, Jan. 2022, ISSN: 13598368. DOI: 10.1016/j.compositesb.2021.109450.
- [19] A. Nair, C. Cai, and X. Kong, “Acoustic emission pattern recognition in CFRP retrofitted RC beams for failure mode identification,” en, *Composites Part B: Engineering*, vol. 161, pp. 691–701, Mar. 2019, ISSN: 13598368. DOI: 10.1016/j.compositesb.2018.12.120.
- [20] M. Barbosh, K. Dunphy, and A. Sadhu, “Acoustic emission-based damage localization using wavelet-assisted deep learning,” en, *J Infrastruct Preserv Resil*, vol. 3, no. 1, p. 6, Apr. 2022, ISSN: 2662-2521. DOI: 10.1186/s43065-022-00051-8.
- [21] A. Abbassi, N. Römgers, F. F. Tritschel, N. Penner, and R. Rolfes, “Evaluation of machine learning techniques for structural health monitoring using ultrasonic guided waves under varying temperature conditions,” en, *Structural Health Monitoring*, vol. 22, no. 2, pp. 1308–1325, Mar. 2023, ISSN: 1475-9217, 1741-3168. DOI: 10.1177/14759217221107566.

- [22] C. Schnur, P. Goodarzi, Y. Lugovtsova, *et al.*, “Towards Interpretable Machine Learning for Automated Damage Detection Based on Ultrasonic Guided Waves,” en, *Sensors*, vol. 22, no. 1, p. 406, Jan. 2022, ISSN: 1424-8220. DOI: 10.3390/s22010406.
- [23] Z. Yang, H. Yang, T. Tian, *et al.*, “A review on guided-ultrasonic-wave-based structural health monitoring: From fundamental theory to machine learning techniques,” en, *Ultrasonics*, vol. 133, p. 107 014, Aug. 2023, ISSN: 0041624X. DOI: 10.1016/j.ultras.2023.107014.
- [24] M. Meo and G. Zumpano, “On the optimal sensor placement techniques for a bridge structure,” *Engineering Structures*, vol. 27, no. 10, pp. 1488–1497, 2005, ISSN: 0141-0296. DOI: <https://doi.org/10.1016/j.engstruct.2005.03.015>.
- [25] G. Suryanarayana, J. Arroyo, L. Helsen, and J. Lago, “A data driven method for optimal sensor placement in multi-zone buildings,” *Energy and Buildings*, vol. 243, p. 110 956, 2021, ISSN: 0378-7788. DOI: <https://doi.org/10.1016/j.enbuild.2021.110956>.
- [26] W. Ostachowicz, R. Soman, and P. Malinowski, “Optimization of sensor placement for structural health monitoring: A review,” *Structural Health Monitoring*, vol. 18, no. 3, pp. 963–988, 2019. DOI: 10.1177/1475921719825601. eprint: <https://doi.org/10.1177/1475921719825601>.
- [27] M. Rautela, J. Senthilnath, J. Moll, and S. Gopalakrishnan, “Combined two-level damage identification strategy using ultrasonic guided waves and physical knowledge assisted machine learning,” en, *Ultrasonics*, vol. 115, p. 106 451, Aug. 2021, ISSN: 0041624X. DOI: 10.1016/j.ultras.2021.106451.
- [28] Z. Zhang and C. Sun, “Structural damage identification via physics-guided machine learning: A methodology integrating pattern recognition with finite element model updating,” en, *Structural Health Monitoring*, vol. 20, no. 4, pp. 1675–1688, Jul. 2021, ISSN: 1475-9217, 1741-3168. DOI: 10.1177/1475921720927488.
- [29] W.-J. Yan, D. Chronopoulos, C. Papadimitriou, S. Cantero-Chinchilla, and G.-S. Zhu, “Bayesian inference for damage identification based on analytical probabilistic model of scattering coefficient estimators and ultrafast wave scattering simulation scheme,” *Journal of Sound and Vibration*, vol. 468, p. 115 083, 2020.
- [30] S. Cantero-Chinchilla, J. Chiachío, M. Chiachío, D. Chronopoulos, and A. Jones, “A robust bayesian methodology for damage localization in plate-like structures using ultrasonic guided-waves,” *Mechanical Systems and Signal Processing*, vol. 122, pp. 192–205, 2019.
- [31] W. Wu, M. Malik, S. Cantero-Chinchilla, *et al.*, “Guided waves-based damage identification in plates through an inverse bayesian process,” *Ultrasonics*, vol. 125, p. 106 773, 2022.
- [32] Q. Li, X. Du, P. Ni, Q. Han, K. Xu, and Z. Yuan, “Efficient bayesian inference for finite element model updating with surrogate modeling techniques,” *Journal of Civil Structural Health Monitoring*, pp. 1–19, 2024.
- [33] A. Marrel and B. Iooss, “Probabilistic surrogate modeling by gaussian process: A review on recent insights in estimation and validation,” *Reliability Engineering & System Safety*, p. 110 094, 2024.

- [34] A. Mishra and A. K. Ray, “Multi-Access Edge Computing assisted ultra-low energy scheduling and harvesting in multi-hop Wireless Sensor and Actuator Network for energy neutral self-sustainable Next-gen Cyber-Physical System,” en, *Future Generation Computer Systems*, vol. 141, pp. 298–324, Apr. 2023, ISSN: 0167739X. DOI: 10.1016/j.future.2022.11.023.
- [35] J. Zander, P. J. Mosterman, T. Padir, Y. Wan, and S. Fu, “Cyber-physical Systems can Make Emergency Response Smart,” en, *Procedia Engineering*, vol. 107, pp. 312–318, 2015, ISSN: 18777058. DOI: 10.1016/j.proeng.2015.06.086.
- [36] Y. Wang, G. Tan, Y. Wang, and Y. Yin, “Perceptual control architecture for cyber-physical systems in traffic incident management,” en, *Journal of Systems Architecture*, vol. 58, no. 10, pp. 398–411, Nov. 2012, ISSN: 13837621. DOI: 10.1016/j.sysarc.2012.06.004.
- [37] K. Monisha and M. Rajasekhara Babu, “A Novel Framework for Healthcare Monitoring System Through Cyber-Physical System,” en, in *Internet of Things and Personalized Healthcare Systems*, Series Title: SpringerBriefs in Applied Sciences and Technology, Singapore: Springer Singapore, 2019, pp. 21–36, ISBN: 9789811308659 9789811308666. DOI: 10.1007/978-981-13-0866-6\_3.
- [38] S. A. Haque, S. M. Aziz, and M. Rahman, “Review of Cyber-Physical System in Healthcare,” en, *International Journal of Distributed Sensor Networks*, vol. 10, no. 4, p. 217 415, Apr. 2014, ISSN: 1550-1477, 1550-1477. DOI: 10.1155/2014/217415.
- [39] D. Tucker, P. Pezzini, and K. M. Bryden, “Cyber-Physical Systems: A New Paradigm for Energy Technology Development,” en, in *Volume 1: Fuels, Combustion, and Material Handling; Combustion Turbines Combined Cycles; Boilers and Heat Recovery Steam Generators; Virtual Plant and Cyber-Physical Systems; Plant Development and Construction; Renewable Energy Systems*, Lake Buena Vista, Florida, USA: American Society of Mechanical Engineers, Jun. 2018, V001T04A001, ISBN: 978-0-7918-5139-5. DOI: 10.1115/POWER2018-7315.
- [40] F. E. Tanha, A. Hasani, S. Hakak, and T. R. Gadekallu, “Blockchain-based cyber physical systems: Comprehensive model for challenge assessment,” en, *Computers and Electrical Engineering*, vol. 103, p. 108 347, Oct. 2022, ISSN: 00457906. DOI: 10.1016/j.compeleceng.2022.108347.
- [41] R. Ch, G. Srivastava, Y. L. V. Nagasree, A. Ponugumati, and S. Ramachandran, “Robust Cyber-Physical System Enabled Smart Healthcare Unit Using Blockchain Technology,” en, *Electronics*, vol. 11, no. 19, p. 3070, Sep. 2022, ISSN: 2079-9292. DOI: 10.3390/electronics11193070.
- [42] W. Doghri, A. Saddoud, and L. Chaari Fourati, “Cyber-physical systems for structural health monitoring: Sensing technologies and intelligent computing,” en, *J Supercomput*, vol. 78, no. 1, pp. 766–809, Jan. 2022, ISSN: 0920-8542, 1573-0484. DOI: 10.1007/s11227-021-03875-5.
- [43] E. Lee, “The Past, Present and Future of Cyber-Physical Systems: A Focus on Models,” en, *Sensors*, vol. 15, no. 3, pp. 4837–4869, Feb. 2015, ISSN: 1424-8220. DOI: 10.3390/s150304837.



- [44] E. R. Griffor, C. Greer, D. A. Wollman, and M. J. Burns, “Framework for cyber-physical systems: Volume 1, overview,” en, National Institute of Standards and Technology, Gaithersburg, MD, Tech. Rep. NIST SP 1500-201, Jun. 2017, NIST SP 1500-201. DOI: 10.6028/NIST.SP.1500-201.
- [45] K. Zhang, Y. Shi, S. Karnouskos, T. Sauter, H. Fang, and A. W. Colombo, “Advancements in Industrial Cyber-Physical Systems: An Overview and Perspectives,” en, *IEEE Trans. Ind. Inf.*, vol. 19, no. 1, pp. 716–729, Jan. 2023, ISSN: 1551-3203, 1941-0050. DOI: 10.1109/TII.2022.3199481.
- [46] H. Fu, Z. Sharif-Khodaei, and M. F. Aliabadi, “An energy-efficient cyber-physical system for wireless on-board aircraft structural health monitoring,” en, *Mechanical Systems and Signal Processing*, vol. 128, pp. 352–368, Aug. 2019, ISSN: 08883270. DOI: 10.1016/j.ymssp.2019.03.050.
- [47] H. Fu, Z. Sharif Khodaei, and M. H. F. Aliabadi, “An Event-Triggered Energy-Efficient Wireless Structural Health Monitoring System for Impact Detection in Composite Airframes,” en, *IEEE Internet Things J.*, vol. 6, no. 1, pp. 1183–1192, Feb. 2019, ISSN: 2327-4662, 2372-2541. DOI: 10.1109/JIOT.2018.2867722.
- [48] C. A. Leckey, M. D. Rogge, and F. Raymond Parker, “Guided waves in anisotropic and quasi-isotropic aerospace composites: Three-dimensional simulation and experiment,” en, *Ultrasonics*, vol. 54, no. 1, pp. 385–394, Jan. 2014, ISSN: 0041624X. DOI: 10.1016/j.ultras.2013.05.007.
- [49] G. Hackmann, Weijun Guo, Guirong Yan, Zhuoxiong Sun, Chenyang Lu, and S. Dyke, “Cyber-Physical Codesign of Distributed Structural Health Monitoring with Wireless Sensor Networks,” en, *IEEE Trans. Parallel Distrib. Syst.*, vol. 25, no. 1, pp. 63–72, Jan. 2014, ISSN: 1045-9219. DOI: 10.1109/TPDS.2013.30.
- [50] Q. Wang, M. Hong, and Z. Su, “A sparse sensor network topologized for cylindrical wave-based identification of damage in pipeline structures,” en, *Smart Mater. Struct.*, vol. 25, no. 7, p. 075015, Jul. 2016, ISSN: 0964-1726, 1361-665X. DOI: 10.1088/0964-1726/25/7/075015.
- [51] R. A. Swartz, J. P. Lynch, S. Zerbst, B. Sweetman, and R. Rolfes, “Structural monitoring of wind turbines using wireless sensor networks,” en, *Smart Structures and Systems*, vol. 6, no. 3, pp. 183–196, Apr. 2010. DOI: 10.12989/SSS.2010.6.3.183.
- [52] L. Qiu, X. Deng, S. Yuan, Y. Huang, and Y. Ren, “Impact Monitoring for Aircraft Smart Composite Skins Based on a Lightweight Sensor Network and Characteristic Digital Sequences,” en, *Sensors*, vol. 18, no. 7, p. 2218, Jul. 2018, ISSN: 1424-8220. DOI: 10.3390/s18072218.
- [53] Song Han, Miao Xie, Hsiao-Hwa Chen, and Yun Ling, “Intrusion Detection in Cyber-Physical Systems: Techniques and Challenges,” en, *IEEE Systems Journal*, vol. 8, no. 4, pp. 1052–1062, Dec. 2014, ISSN: 1932-8184, 1937-9234, 2373-7816. DOI: 10.1109/JSYST.2013.2257594.
- [54] E. Hüllermeier and W. Waegeman, “Aleatoric and epistemic uncertainty in machine learning: An introduction to concepts and methods,” en, *Mach Learn.*, vol. 110, no. 3, pp. 457–506, Mar. 2021, ISSN: 0885-6125, 1573-0565. DOI: 10.1007/s10994-021-05946-3.

- [55] A. Mosallam, “Strength and ductility of reinforced concrete moment frame connections strengthened with quasi-isotropic laminates,” en, *Composites Part B: Engineering*, vol. 31, no. 6-7, pp. 481–497, Oct. 2000, ISSN: 13598368. DOI: 10.1016/S1359-8368(99)00068-2.
- [56] H. Ullah, A. R. Harland, and V. V. Silberschmidt, “Dynamic bending behaviour of woven composites for sports products: Experiments and damage analysis,” en, *Materials & Design*, vol. 88, pp. 149–156, Dec. 2015, ISSN: 02641275. DOI: 10.1016/j.matdes.2015.08.147.
- [57] “Performance measures for systems under multiple environments,” en, *IEEE/CAA J. Autom. Sinica*, vol. 3, no. 1, pp. 90–95, Jan. 2016, ISSN: 2329-9266, 2329-9274. DOI: 10.1109/JAS.2016.7373766.
- [58] L. C. Mostaço-Guidolin, R. B. Frigori, L. Ruchko, and R. M. Galvão, “Scte: An open-source perl framework for testing equipment control and data acquisition,” *Computer Physics Communications*, vol. 183, no. 7, pp. 1511–1518, 2012, ISSN: 0010-4655. DOI: <https://doi.org/10.1016/j.cpc.2012.02.013>.
- [59] B. Feng, A. L. Ribeiro, and H. G. Ramos, “Using guided ultrasonic wave inspection to quantify the length of delaminations in composite laminates,” in *AIP Conference Proceedings*, AIP Publishing, vol. 1949, 2018.
- [60] K. O’Shea and R. Nash, *An Introduction to Convolutional Neural Networks*, en, arXiv:1511.08458 [cs], Dec. 2015.
- [61] F. Bai, D. Gagar, P. Foote, and Y. Zhao, “Comparison of alternatives to amplitude thresholding for onset detection of acoustic emission signals,” en, *Mechanical Systems and Signal Processing*, vol. 84, pp. 717–730, Feb. 2017, ISSN: 08883270. DOI: 10.1016/j.ymssp.2016.09.004.
- [62] A. H. Abdulaziz, M. Hedaya, A. Elsabbagh, K. Holford, and J. McCrory, “Acoustic emission wave propagation in honeycomb sandwich panel structures,” en, *Composite Structures*, vol. 277, p. 114580, Dec. 2021, ISSN: 02638223. DOI: 10.1016/j.compstruct.2021.114580.
- [63] J. E. Cavanaugh and A. A. Neath, “The Akaike information criterion: Background, derivation, properties, application, interpretation, and refinements,” en, *WIREs Computational Statistics*, vol. 11, no. 3, e1460, May 2019, ISSN: 1939-5108, 1939-0068. DOI: 10.1002/wics.1460.
- [64] A. St-Onge, “Akaike information criterion applied to detecting first arrival times on microseismic data,” en, in *SEG Technical Program Expanded Abstracts 2011*, Society of Exploration Geophysicists, Jan. 2011, pp. 1658–1662. DOI: 10.1190/1.3627522.
- [65] P. Sedlak, P. Sedlak, Y. Hirose, M. Enoki, and J. Sikula, “Arrival time detection in thin multilayer plates on the basis of Akaike information criterion,” en, 2008.
- [66] M. Philibert, C. Soutis, M. Gresil, and K. Yao, “Damage Detection in a Composite T-Joint Using Guided Lamb Waves,” en, *Aerospace*, vol. 5, no. 2, p. 40, Apr. 2018, ISSN: 2226-4310. DOI: 10.3390/aerospace5020040.
- [67] H. Mei, R. James, M. F. Haider, and V. Giurgiutiu, “Multimode Guided Wave Detection for Various Composite Damage Types,” en, *Applied Sciences*, vol. 10, no. 2, p. 484, Jan. 2020, ISSN: 2076-3417. DOI: 10.3390/app10020484.

- [68] C. Willberg, S. Koch, G. Mook, J. Pohl, and U. Gabbert, “Continuous mode conversion of Lamb waves in CFRP plates,” en, *Smart Mater. Struct.*, vol. 21, no. 7, p. 075 022, Jul. 2012, issn: 0964-1726, 1361-665X. DOI: 10.1088/0964-1726/21/7/075022.